Electronic Supporting Information for: Side-on Cupric-Superoxo triplet complexes as competent agents for H-abstraction relevant to the active site of PHM

Brenda N. Sánchez-Eguía,[a] Marcos Flores-Alamo,[b] Maylis Orio,[c,d] Ivan Castillo*[a]

[a] *Instituto de Química, Universidad Nacional Autónoma de México, Circuito Exterior, CU, México DF, 04510, México*

[b] *Facultad de Química, División de Estudios de Posgrado, Universidad Nacional Autónoma de México, Circuito Exterior, CU, México DF, 04510, México*

[c] *Laboratoire de Spectrochimie Infrarouge et Raman, Université des Sciences et Technologies de Lille, UMR CNRS 8516, 59655 Villeneuve d'Ascq Cedex, France*

[d] *Institut des Sciences Moléculaires de Marseille, Aix Marseille Université, UMR 7313, Avenue Escadrille Normandie-Niémen, 13397 Marseille Cedex 20, France*

EXPERIMENTAL

1. Materials and methods

General. Air-sensitive compounds were manipulated under an atmosphere of dinitrogen in a glovebox or by vacuum-line and Schlenk techniques. Solvents were dried by standard methods and distilled under N_2 prior to use. $Cu(OTf)_2$ (OTf^- = $CF_3SO_3^-$) CuCl, $Cu(ClO_4)_2 \cdot 6H_2O$, hydrogen peroxide, triethylamine, Na_2EDTA, and 9,10-dihydroanthracene (9,10-DHA) were used as received from Aldrich Chemical Co. $[Cu(CH_3CN)_4]OTf$ was prepared according to the literature procedure.[1] Preparation of $\mathbf{L^1}$ and $\mathbf{L^2}$ has been previously reported.[2]

Instrumental. Bench-top low temperature UV–visible experiments were carried out on an Agilent spectrophotometer model 8453 equipped with a liquid nitrogen chilled Unisoku USP-203-A cryostat using a 1 cm modified Schlenk cuvette. Melting points were determined on an Electrothermal Mel-Temp apparatus and are uncorrected. Infrared spectra were recorded with a Bruker Tensor 27 spectrophotometer in the 4000–400 cm^{-1} region as KBr disks. NMR spectra were recorded on a JEOL Eclipse 300 spectrometer in $CDCl_3$ with tetramethylsilane as an internal standard, or in CD_3CN referenced relative to the residual solvent protons at 300 (^1H) or 75 MHz (^{13}C) or a Bruker Avance III at 400 MHz for variable temperature ^1H NMR measurements. Mass spectra were obtained on a Bruker Daltonics Esquire 6000 spectrometer with ion trap (Electrospray). Elemental analyses were performed at the microanalytical facility of the Instituto de Química, or USAI –Facultad de Química. GC-MS determinations were performed using an Agilent 5975C instrument equipped with a 30 m DB-5MS capillary (0.32 mm i.d.) column in CH_2Cl_2. EPR measurements were done at room temperature or 77 K in quartz tubes with a Jeol JES-TE300 spectrometer at X band frequency (9.4 GHz) at 100 KHz field modulation, with a cylindrical cavity (TE011 mode).

X-Ray crystallography. Single crystals were mounted on a Bruker Smart diffractometer equipped with an Apex CCD area detector, or an Oxford Diffraction Gemini A

diffractometer with a CCD area detector. Frames were collected by omega scans, and integrated with the Bruker SAINT software package using the appropriate unit cell in the case of the former diffractometer,[3] and the CRYSALIS PRO and CRYSALIS RED software packages for data collection and data integration with the latter.[4] The structures were solved using the SHELXS-97 program,[5] and refined by full-matrix least-squares on F^2 with SHELXL-97.[6] Weighted R-factors, R_w, and all goodness of fit indicators, S, were based on F^2. The observed criterion of ($F^2 > 2\sigma F^2$) was used only for calculating the R-factors. All non-hydrogen atoms were refined with anisotropic thermal parameters in the final cycles of refinement. Hydrogen atoms were placed in idealised positions, with C–H distances of 0.93 Å and 0.98 Å for sp^2 and sp^3 hybridised carbon atoms, respectively. The isotropic thermal parameters of the hydrogen atoms were assigned the values of U_{iso} = 1.2 times the thermal parameters of the parent non-hydrogen atom.

2. Synthesis of copper(I/II) complexes

[$\mathbf{L^1}Cu^{II}(EtOH)](OTf)_2$. In a 100 mL round bottom flask, 100 mg (0.21 mmol) of $\mathbf{L^1}$ was disolved in 20 mL of distilled ethanol and 77 mg (0.21 mmol) of the $Cu(OTf)_2$ were added to the solution after 5 min of stirring at room temperature, the reaction mixture turned deep green. After 23 hrs of stirring, 20 mL of diethyl ether were added and the complex precipitated as a deep green solid, which was dried under vacuum to afford 133 mg of copper (II) complex (75%). Mp.: 158-160°C. IR (KBr): ν = 3233, 2957, 1615, 1599, 1530, 1501, 1485, 1455, 1324, 1273, 1241, 1156, 1054, 1026, 935, 812, 746, 705, 634, 572, 545, 514, 432 cm^{-1}. ESI-MS: $[\mathbf{L^1}]^+$ = 469.9 m/z; $[\mathbf{L^1}Cu]^+$ = 531.9 m/z; $[\mathbf{L^1}Cu(C_2H_5OH)]^+$ = 577.9 m/z; $[\mathbf{L^1}CuCF_3SO_3]^+$ = 680.8 m/z. UV-vis (0.3 mM, THF, rt): λ = 313 nm S→Cu^{II}, ε = 1710 $M^{-1}cm^{-1}$; λ = 712 nm *d-d*, ε = 123 M^{-1} cm^{-1}. ESR (77 K, CH_3CN): $g_{\parallel}$ = 2.249; $g_{\perp}$ = 2.064; $A_{\parallel}$ = 167 G. Elemental Analysis calculated for $C_{32}H_{37}CuF_6N_5O_7S_3$ ([$\mathbf{L^1}Cu^{II}(EtOH)](OTf)_2$): C, 43.80; H, 4.25; N, 7.98; found: C, 44.11; H, 4.02; N, 8.59.

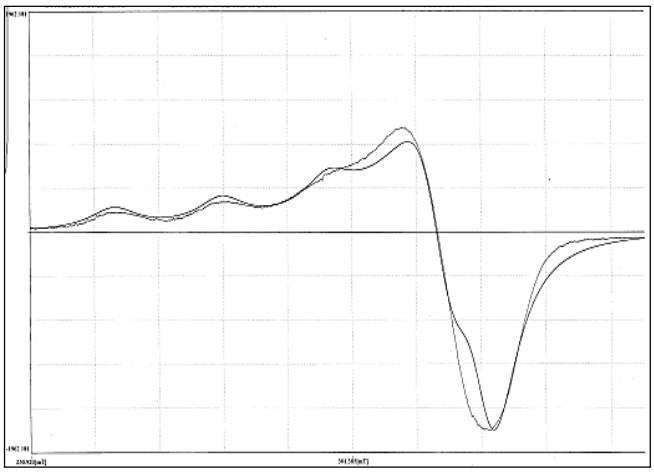

Figure S1. Experimental and simulated ESR spectra of $\mathbf{L^1}Cu^{II}(OTf)_2$ (77 K, CH_3CN).

L^2CuCl. To a solution of L^2 (186 mg, 0.49 mmol) in 5 mL CH_3CN was added CuCl (49 mg, 0.49 mmol), and the mixture was stirred under N_2 for 3 h. A colourless solid started to deposit, and addition of 2 mL of diethylether and filtration afforded 150 mg (64%) of L^2CuCl as colourless microcrystals. Mp: 132-135°C. Elemental Analysis Calculated for $C_{21}H_{25}ClCuN_5S$ (L^2CuCl): C 52.71, H 5.27, N, 14.64; found C 52.84, H 5.34, N 14.19.

$[L^2Cu]_2(OTf)_2$. To a solution of L^2 (140 mg, 0.49 mmol) in 5 mL THF was added $[Cu(CH_3CN)_4]OTf$ (130 mg, 0.49 mmol), and the mixture was stirred under N_2 for 3 h. Volatiles were then evaporated under reduced pressure, and addition of ca. 3 mL of diethylether and filtration afforded 96 mg (45%) of L^2Cu(OTf) as colourless microcrystals. Mp: 157-159°C. ^{1}H NMR (300 MHz, THF-d_8): δ = 7.61 (d, ^3J = 64.7 Hz 2 H, BzIm), 7.47 (d, ^3J = 64.7 Hz, 2 H, BzIm), 7.2 (m, 4 H, BzIm), 4.45 (s, 4 H, BzImCH_2), 3.78 (s, 6 H, NCH_3), 3.62 (s, 2 H, NCH_2), 2.78 (s, 2 H, SCH_2), 1.93 (s, 3 H, SCH_3) ppm. IR (KBr): ν = 3521, 3212, 3060, 2922, 2854, 1672, 1614, 1502, 1480, 1455, 1373, 1327, 1254, 1154, 1086, 1026, 936, 869, 801, 746, 698, 635, 572, 549, 515, 466, 432 cm^{-1}. Elemental Analysis calculated for $C_{22}H_{25}CuF_3N_5O_3S_2$ (L^2Cu(OTf) •2CH_3CN): C 46.32, H, 4.63, N, 14.54; found C 46.35, H 4.34, N 14.09.

$[L^2Cu^{II}Cl]ClO_4$. In a 100 mL round bottom flask, 100 mg (0.26 mmol) of L^2 were dissolved in 20 mL of distilled ethanol, and 93 mg (0.26 mmol) of $Cu(ClO)_4 \cdot 6H_2O$ were added to the solution; after 5 min of stirring at room temperature, the reaction mixture turned greenish blue. After 3 hrs of stirring, 20 mL of diethyl ether were added and the complex precipitated as a turquoise solid, which was dried under vacuum to afford 154 mg (89%) of $[L^2Cu^{II}Cl]ClO_4$. Mp. 223-225°C. IR (KBr): ν = 3467, 3356, 3099, 3035, 2975, 1614, 1504, 1454, 1362, 1323, 1296, 1251, 1079, 932, 911, 778, 749, 706, 620, 544, 506, 464, 430 cm^{-1}. ESI-MS: $[L^2Cu]^+$ = 441.8 m/z; $[L^2CuCl]^+$ = 476.8 m/z; $[L^2CuClO_4]^+$ = 540.8 m/z; $[(L^2+H)CuCl(ClO_4)]^+$ = 576.9 m/z. UV-vis (0.3 mM, CH_3CN, rt): λ = 326 nm S→Cu^{II}, ε = 1201 M^{-1}cm^{-1}; λ = 665 nm *d-d*, ε = 92 M^{-1}cm^{-1}. ESR (77 K, CH_3CN): $g_{\parallel}$ = 2.244; $g_{\perp}$ = 2.072; $A_{\parallel}$ = 167 G. Elemental Analysis calculated for $C_{21}H_{27}Cl_2CuN_5O_5S$ ($[L^2Cu^{II}Cl]ClO_4 \cdot H_2O$): C, 42.32; H, 4.57; N, 11.75; found: C, 42.74; H, 3.89; N, 12.04. Turquoise X-ray quality crystals were obtained by slow evaporation of a concentrated acetonitrile solution.

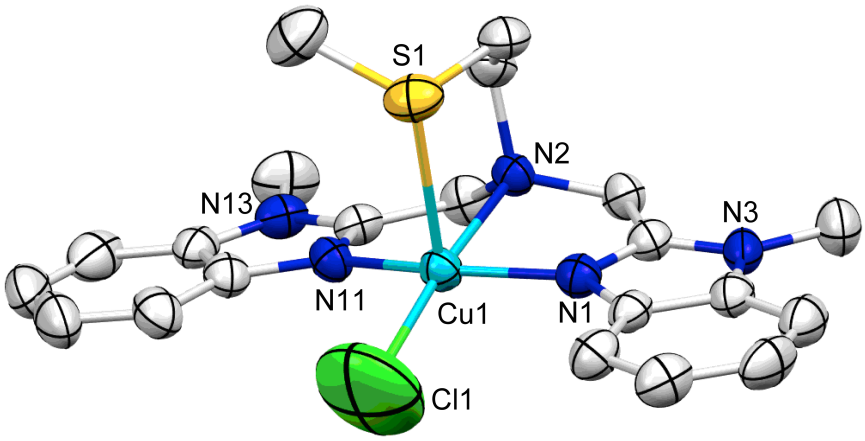

Figure S2. Mercury diagram of $[\mathbf{L}^{2}Cu^{II}Cl]^{+}$ at the 50% probability level; H-atoms and disordered perchlorate anion are omitted for clarity. Selected bond distances (Å): Cu1-Cl1 2.280(9), Cu1-S1 2.686(2), Cu1-N1 1.963(4), Cu1-N2 2.141(3), Cu1-N11 1.965(3); angles (°): Cl1-Cu1-S1 102.0(3), Cl1-Cu1-N1 97.7(3), Cl1-Cu1-N2 172.1(3), Cl1-Cu1-N11 98.0(3), S1-Cu1-N1 88.1(1), S1-Cu1-N2 85.8(1), S1-Cu1-N11 101.2(1), N1-Cu1-N2 81.9(1), N1-Cu1-N11 159.7(2), N2-Cu1-N11 80.8(1).

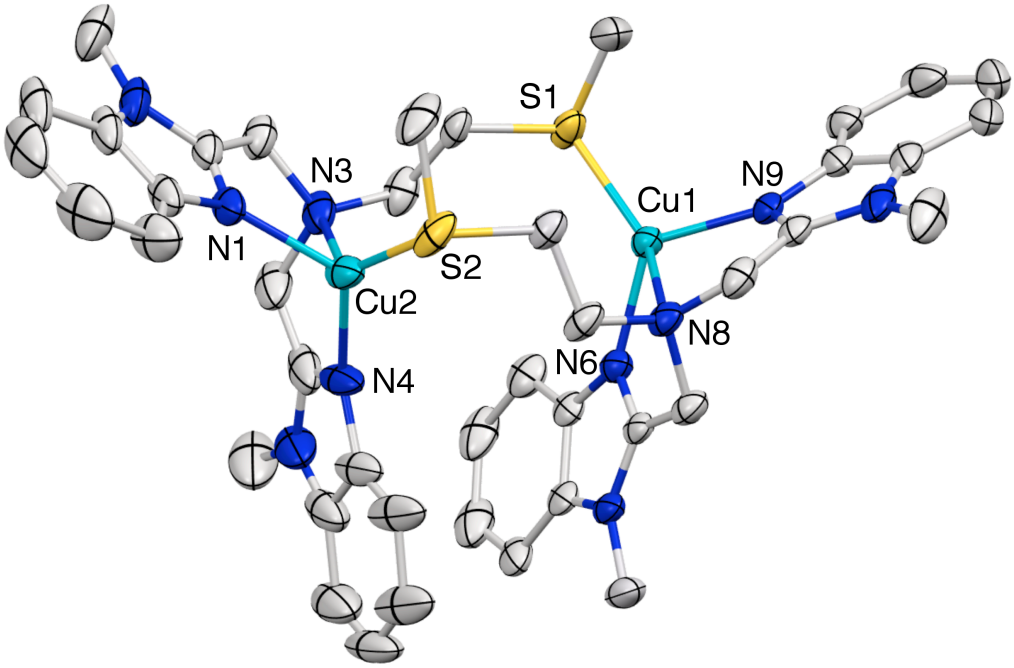

Figure S3. Mercury diagram of $[\mathbf{L}^{2}Cu]_2OTf_2$ at the 50% probability level; H-atoms and disordered triflate anions are omitted for clarity. Selected bond distances (Å): Cu1-S1 2.211(2), Cu1-N6 1.987(6), Cu1-N8 2.458(6), Cu1-N9 2.015(5), Cu2-S2 2.188(2), Cu2-N1 2.035(3), Cu2-N3 2.437(6), Cu2-N4 1.996(7); angles (°): S1-Cu1-N6 122.5(2), S1-Cu1-N8 135.3(1), S1-Cu1-N9 113.6(2), N6-Cu1-N8 76.5(2), N6-Cu1-N9 121.7(2), N8-Cu1-N9 74.8(2), S2-Cu2-N1 111.7(2), S2-Cu2-N3 132.3(1), S2-Cu2-N4 130.8(2), N1-Cu2-N3 74.3(2), N1-Cu2-N4 114.7(2), N3-Cu2-N4 76.8(2).

3. Spectroscopic data for copper complexes

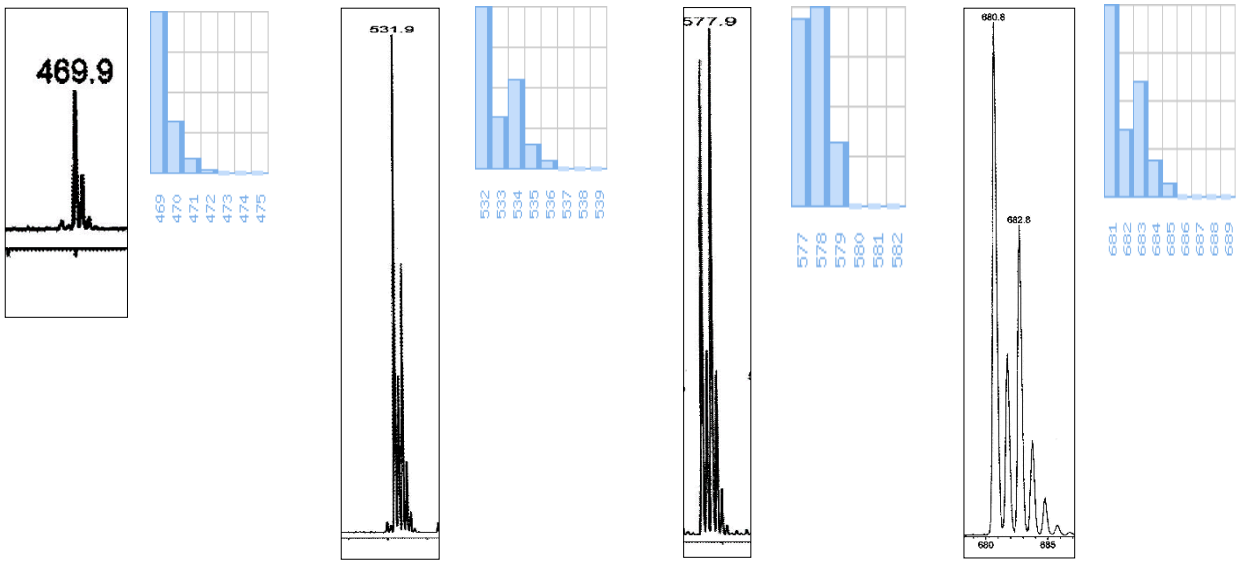

Figure S4. ESI-MS and simulation of $\mathbf{L^1}Cu^{II}(OTf)_2(CH_3CN)$.

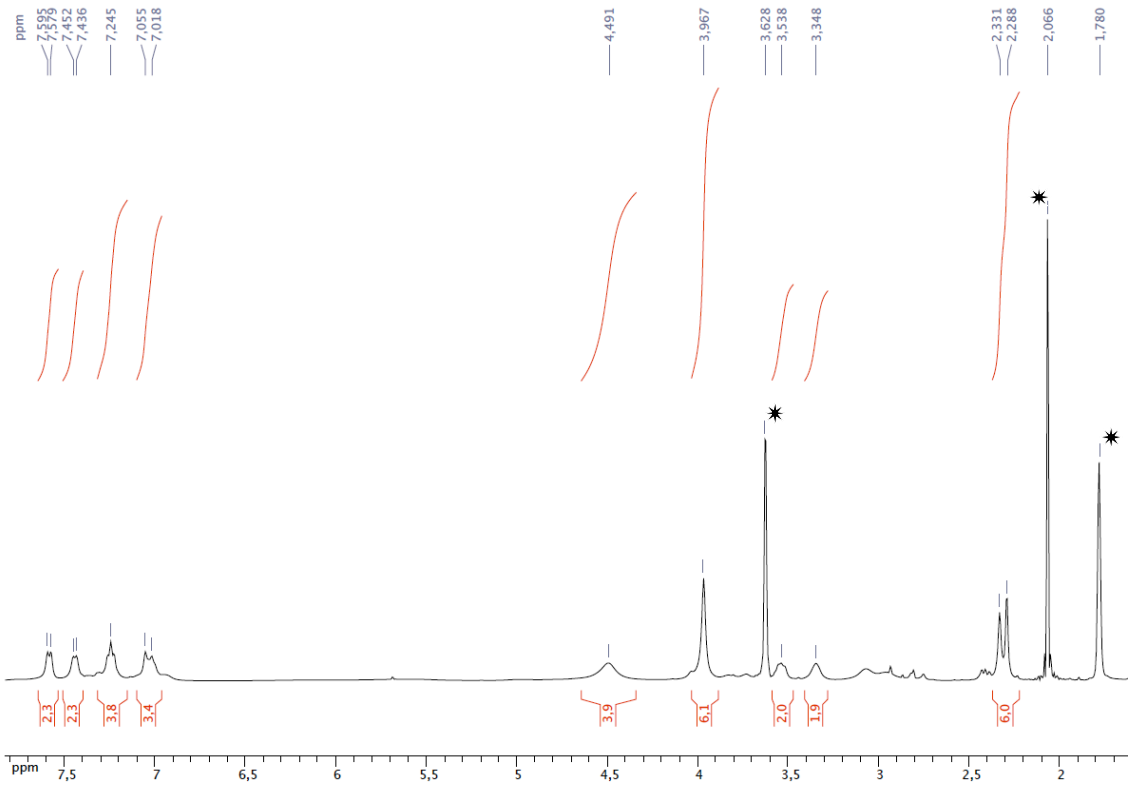

Figure S5. ^{1}H NMR spectrum of [$\mathbf{L^1}$Cu]OTf at -40°C in THF-d_8 (*residual solvent peaks).

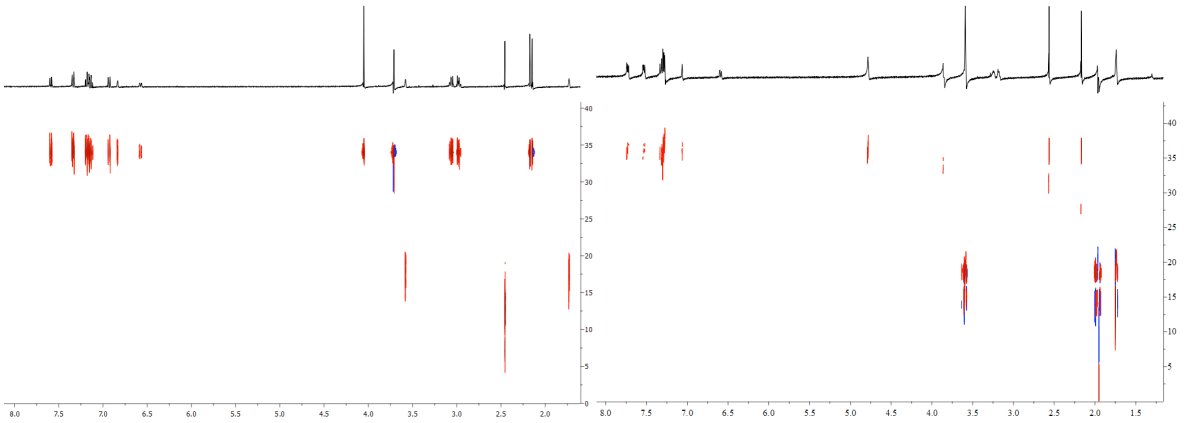

Figure S6. Comparison of DOSY NMR spectra of $\mathbf{L^1}$ (left) and [$\mathbf{L^1}$Cu]OTf (right) in THF-d_8 at 25°C, showing comparable diffusion coefficients (3.3 mM solutions).

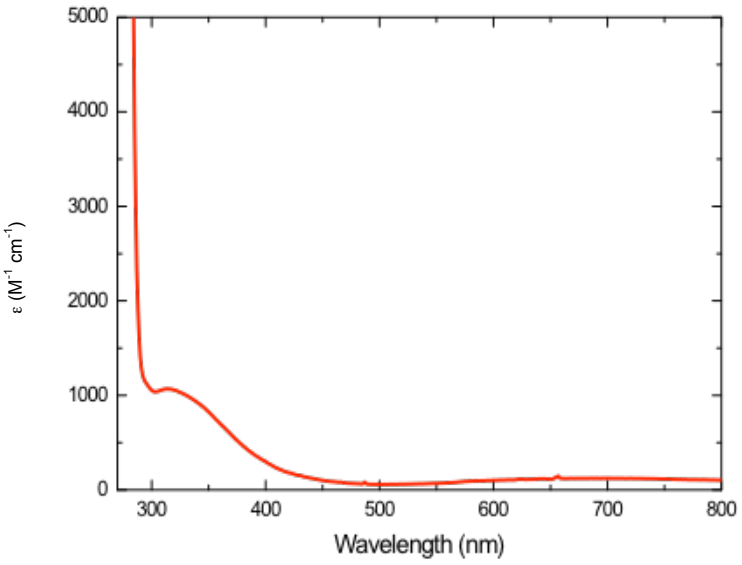

Figure S7. UV-vis spectrum of $\mathbf{L^1}Cu^{II}(OTf)_2$ (THF, RT).

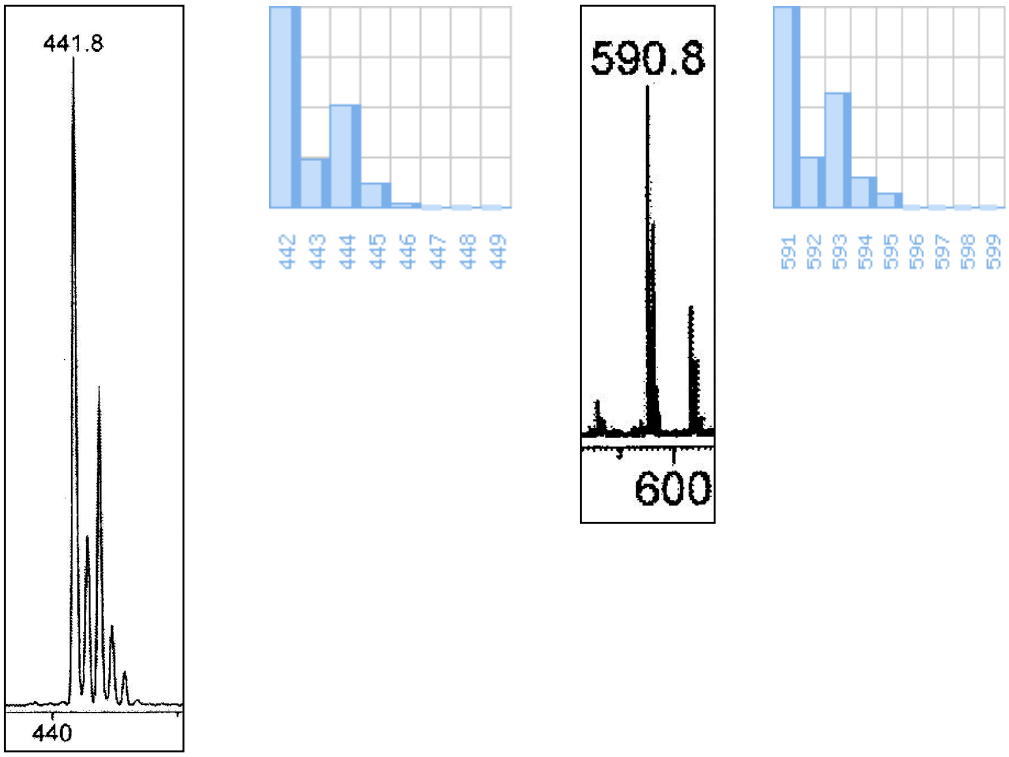

Figure S8. ESI-MS and simulation of [$\mathbf{L}^{2}$Cu]OTf.

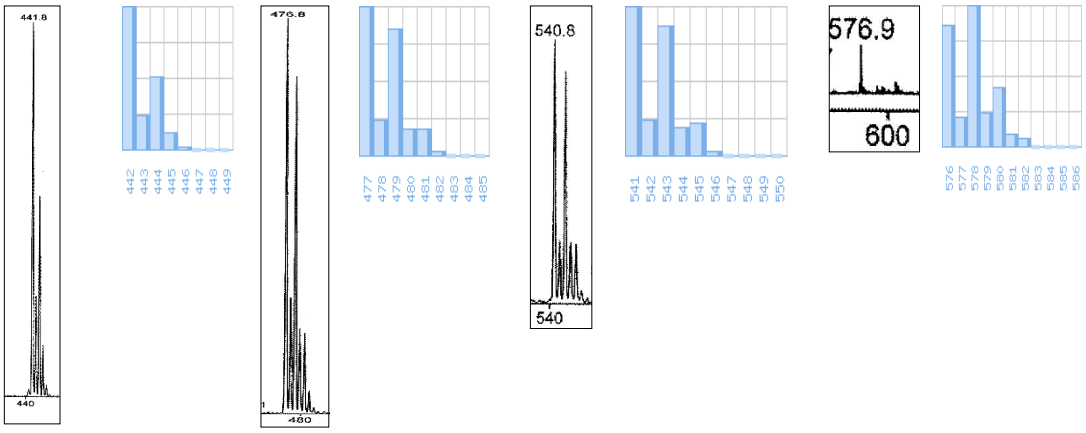

Figure S9. ESI-MS and simulation of [$\mathbf{L}^{2}Cu^{II}Cl]ClO_4(CH_3CN)$.

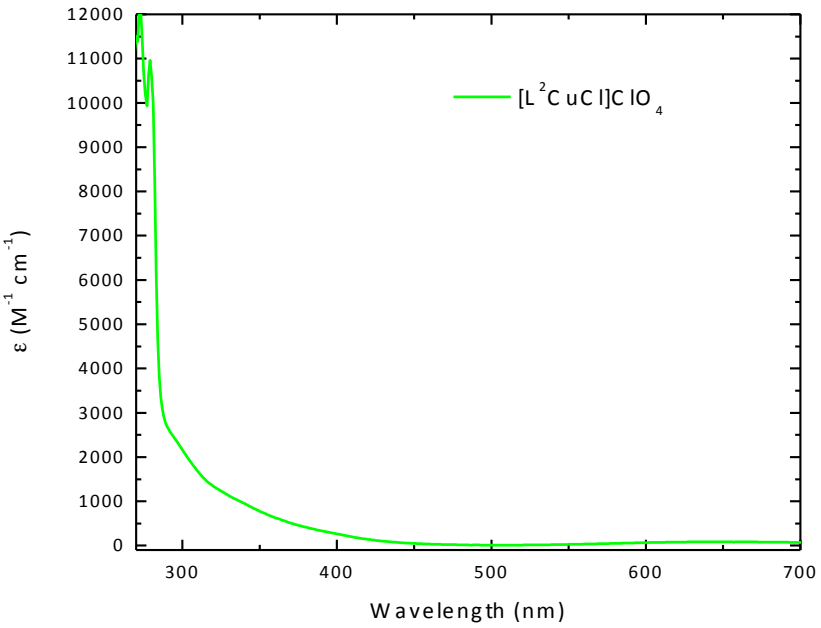

Figure S10. UV-vis spectrum of [$\mathbf{L^2}Cu^{II}Cl]ClO_4$ (CH_3CN, RT).

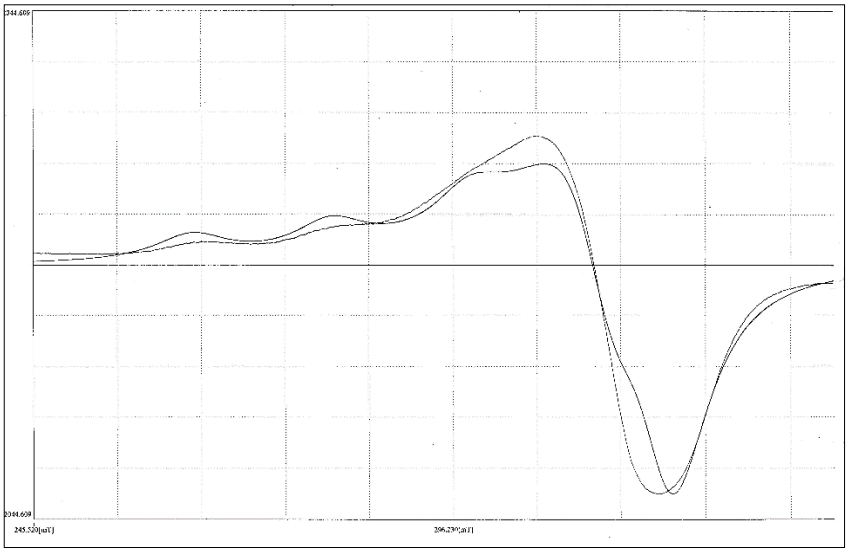

Figure S11. Experimental and simulated ESR spectra of [$\mathbf{L^2}Cu^{II}Cl]ClO_4$ (77 K, CH_3CN).

Table S1. Selected crystallographic data.

	$\mathbf{L}^2$CuCl	$[\mathbf{L}^1Cu]_2(OTf)_2$•2THF	$[\mathbf{L}^2Cu^{II}Cl]ClO_4$	$[\mathbf{L}^1Cu^{II}(\mu\text{-}OH)]_2OTf_2$
Formula	$C_{21}H_{25}ClCuN_5S$	$C_{52}H_{66}Cu_2F_6N_{10}O_8S_4$	$C_{21}H_{25}Cl_2CuN_5O_4S$	$C_{58}H_{64}Cu_2F_6N_{10}O_8S_4$
Molecular weight	478.51	1328.46	577.9	1398.51
Crystal system	Monoclinic	Monoclinic	Monoclinic	Monoclinic
Space group	P 21/n	C 2/c	P 21/c	P 21/n
Wavelength (Å)	0.71073	0.71073	0.71073	1.54184
Crystal color	Colourless	Pale grey	Blue	Blue
T (K)	173(2)	130(2)	298(2)	130 (2)
Crystal size (mm)	0.10 × 0.32 × 0.33	0.33 × 0.22 × 0.21	0.39 × 0.26 × 0.15	0.45 x 0.20 x 0.14
a (Å)	11.2265(11)	47.532(4)	8.1746(4)	11.6838(4)
b (Å)	14.2640(14)	11.8821(5)	23.0559(9)	26.1913(11)
c (Å)	12.7921(12)	29.711(2)	13.4166(6)	15.5908(7)
α (°)	90	90	90	90
β (°)	97	135	103	111
γ (°)	90	90	90	90
V (Å^3)	2032.2(3)	11766(3)	2462.94(19)	4431.8(3)
hkl ranges	-13 ≤ h ≤ 13 -17 ≤ k ≤ 17 -15 ≤ l ≤ 15	-51 ≤ h ≤ 57 -14 ≤ k ≤ 10 -35 ≤ l ≤ 35	-8 ≤ h ≤ 9 -25 ≤ k ≤ 27 -16 ≤ l ≤ 16	-14 ≤ h ≤ 11 -32 ≤ k ≤ 32 -19 ≤ l ≤ 19
ρ_{calc} (g cm^{-3})	1.564	1.500	1.619	1.048
Z	4	8	2	2
F(000)	992	5504	1224	1444
μ (mm^{-1})	1.328	0.945	1.984	1.951
θ range (°)	2.28 to 25.36	3.675 to 29.063	2.36 to 22.00	4.048 to 68.358
Absorption corr.	Analytical	Analytical	Analytical	Analytical
T_{max}, T_{min}	0.8785, 0.6304	0.835, 0.79	0.8724, 0.7759	0.32, 0,629
Refinement	Full-matrix least-squares on F^2	Full-matrix least-squares on F^2	Full-matrix least-squares on F^2	Full-matrix least-squares on F^2
Reflections	3715	9515	8786	8828
Data/restr./param.	3715/0/265	10746/389/733	4488/186/357	8828/1/381
Goodness-of-fit	1.044	1.028	0.926	0.94
R	0.0313	0.0650	0.0485	0.0999
R_w	0.0779	0.1569	0.1076	0.1917
Peak, hole (e Å^3)	0.321, – 0.580	1.056, –0.823	0.878, –0.607	0.831, -0.447

4. Reactivity studies

Generation of superoxo copper complexes. In the glovebox from a 1 mM stock solution, 0.3 mM Cu^+ complexes solutions were prepared in 10 mL THF or 2-MeTHF. 4 mL of this solution were transferred into a 1 cm Schlenk cuvette, which was sealed with a rubber septum. The cell was transferred to the pre-cooled cryostat and chilled at –100 or –80°C (THF), –125°C (2-MeTHF) with 10 minutes allowed for equilibration prior to oxygenation. Dioxygen was gently bubbled through the solution using a long needle for 40 seconds forming $[(\mathbf{L}^1/\mathbf{L}^2)Cu^{II}–OO^{\bullet-}]^+$.

Generation of hydroperoxo copper complexes. In the glovebox from a 1 mM stock solution, 0.3 mM Cu^{2+} complexes solutions were prepared in 10 mL THF. 4 mL of this solution were transferred into a 1 cm Schlenk cuvette, which was sealed with a rubber septum. The cell was transferred to the UV-vis spectrophotometer and 10 equiv of a 1:1 H_2O_2/Et_3N solution were added. After the addition the formation of $[(\mathbf{L^1}/\mathbf{L^2})Cu^{II}–OOH]^+$ was monitored for 1 hr.

5. Characterisation of superoxo complexes

The UV-vis spectra of superoxo complexes with both ligands were determined in THF and 2-MeTHF at -100/-80 and -125°C respectively:

$[\mathbf{L^1}Cu^{II}–OO^{\bullet-}]^+$. UV-vis (-100°C, THF): λ = 336 nm ε = 1529 M^{-1} cm^{-1}, *d-d* λ = 614 nm ε = 285 M^{-1} cm^{-1}.

$[\mathbf{L^2}Cu^{II}–OO^{\bullet-}]^+$ UV-vis (-100°C, THF): λ = 339 nm, ε = 2318 M^{-1} cm^{-1}, *d-d* λ = 609 nm, ε = 119 M^{-1} cm^{-1}. UV-vis (-125°C, 2-MeTHF): λ = 340 nm, ε = 2220 M^{-1} cm^{-1}.

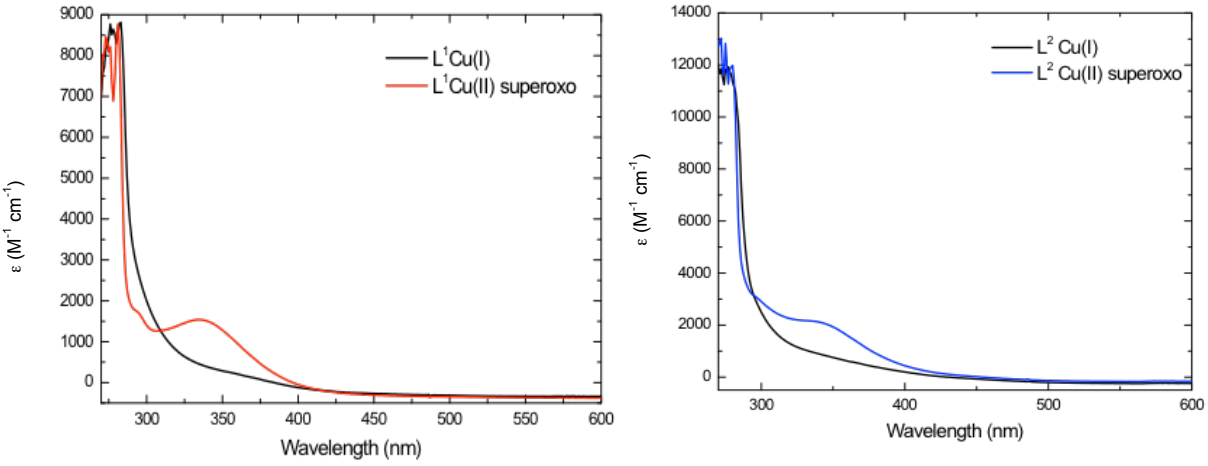

Figure S12. UV-vis spectra of $[\mathbf{L^1}Cu^{II}–OO^{\bullet-}]^+$ in THF at -100°C (left), and $[\mathbf{L^2}Cu^{II}–OO^{\bullet-}]^+$ in 2-MeTHF at -125°C (right).

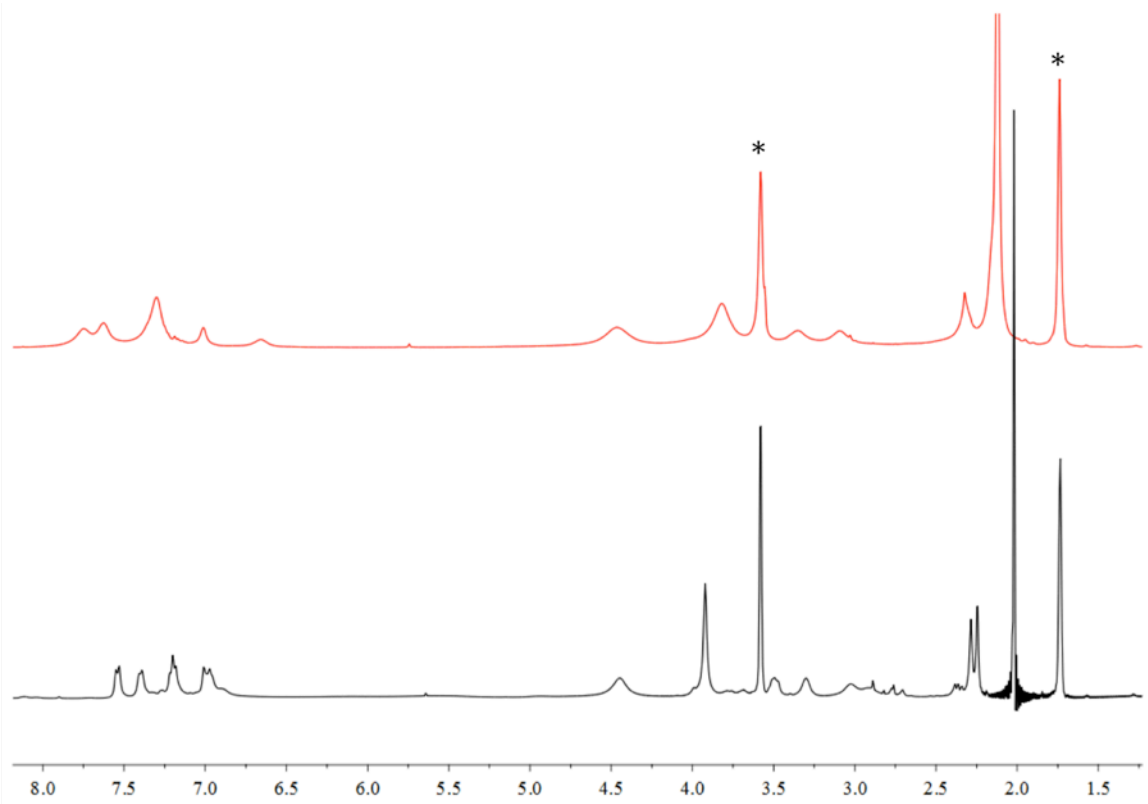

Figure S13. Top: ^{1}H NMR spectrum of [**L**^{1}Cu]OTf + O_2 at -80°C in THF-d_8, bottom: ^{1}H NMR spectrum before oxygenation (same as in **Fig. S5**, *residual solvent peaks).

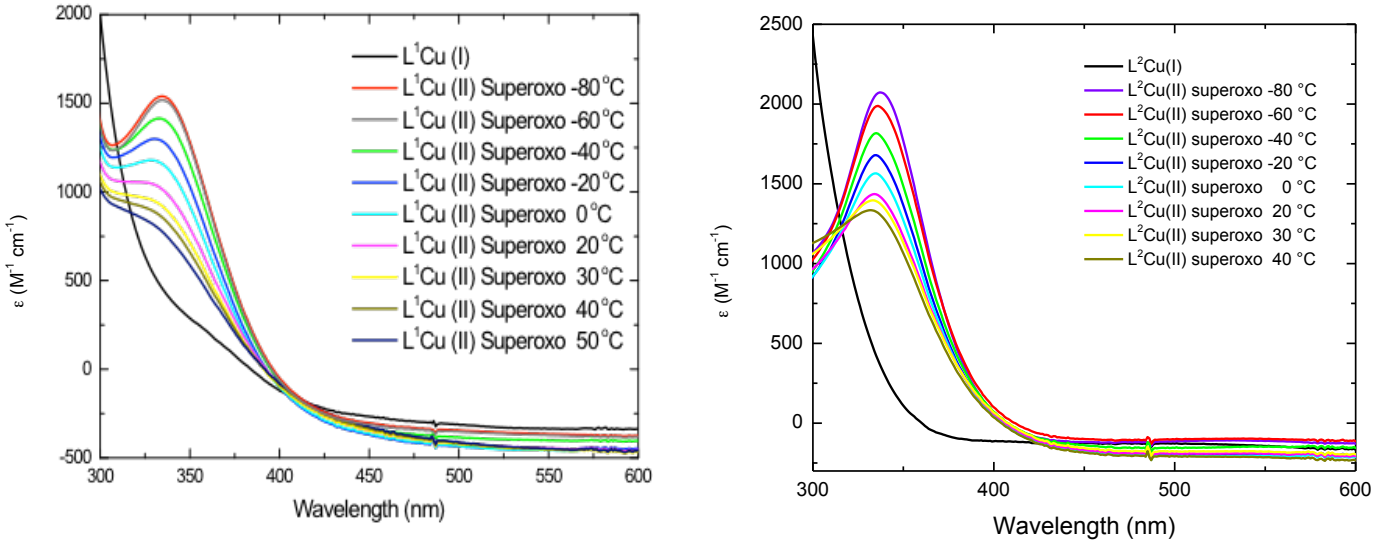

Figure S14. Variable-temperature UV-vis spectra of thermal decomposition of [(**L**^{1} (left)/**L**^{2} (right))Cu^{II}–$OO^{\bullet-}$]$^{+}$ in THF.

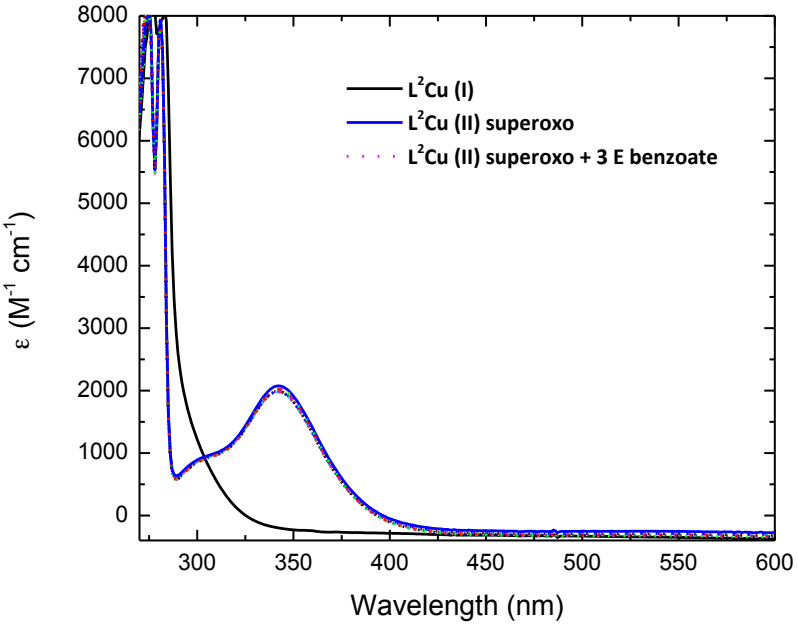

Figure S15. UV-vis spectra of $\mathbf{L^2}Cu(II)O^{\cdot-}_2$ with 3 eq. of tetramethylammonium benzoate (THF at -80°C).

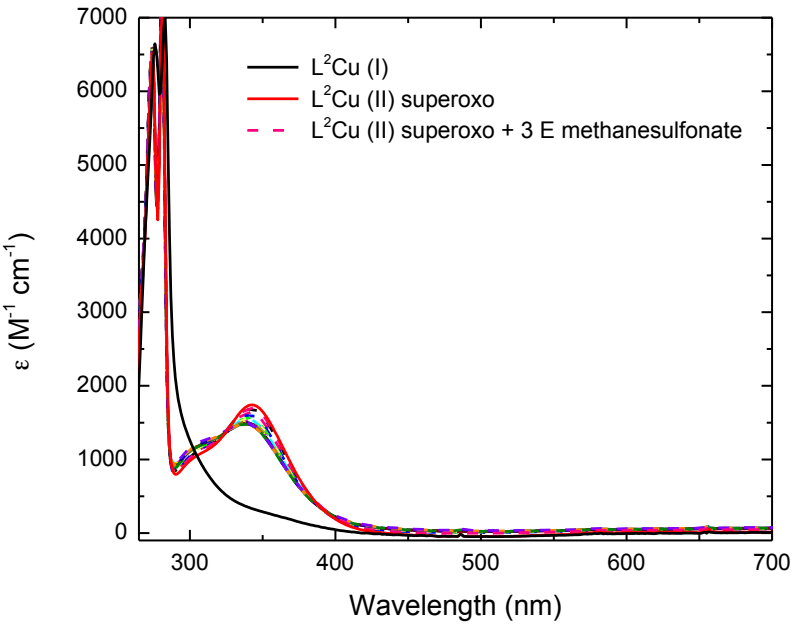

Figure S16. UV-vis spectra of $\mathbf{L^2}Cu(II)O^{\cdot-}_2$ with 3 eq. of tetrabutylammonium methanesulfonate (THF at -80°C).

6. DFT Calculations

All theoretical calculations were based on the Density Functional Theory (DFT) and were performed with the ORCA software package.[7] Full geometry optimisations were carried out for all complexes using the GGA functional BP86[8-10] in combination with the TZV/P[11] basis set for all atoms and by taking advantage of the resolution of the identity (RI) approximation in the Split-RI-J variant[12] with the appropriate Coulomb fitting sets.[13] Increased integration grids (Grid4 in ORCA convention) and tight SCF convergence criteria were used. Vibrational frequency calculations were performed to ensure that each geometry optimization converged to a real minimum. Solvent effects were accounted for according to the experimental conditions. For that purpose, we used the THF solvent (ε = 7.25) within the framework of the conductor like screening (COSMO) dielectric continuum approach.[14] Optical properties were predicted from additional single-point calculations using the B3LYP[15,16] functional together with the TZV/P basis set. Electronic transition energies and dipole moments for all models were calculated using time-dependent DFT (TD-DFT)[17-19] within the Tamm-Dancoff approximation.[20,21] To increase computational efficiency, the RI approximation[22] was used in calculating the Coulomb term and at least 40 excited states were calculated in each case. Difference transition density plots were generated for each transition and visualized with the Chemcraft program.[23] Energetic analysis was carried out from additional single point high-spin and Broken Symmetry (BS)[24-26] calculations using the B3LYP functional and the TZV/P basis set on the previously optimised geometries. For the BS state, the single-point calculation was performed using the high-spin wave function and the BrokenSym (1,1) keyword to generate the unrestricted broken-symmetry singlet wave function. The Heisenberg isotropic exchange coupling constants J were evaluated from the BS state and the Yamaguchi formula[27,28] was used to estimate the exchange coupling constants J based on the Heisenberg–Dirac–van Vleck Hamiltonian.[29-32]

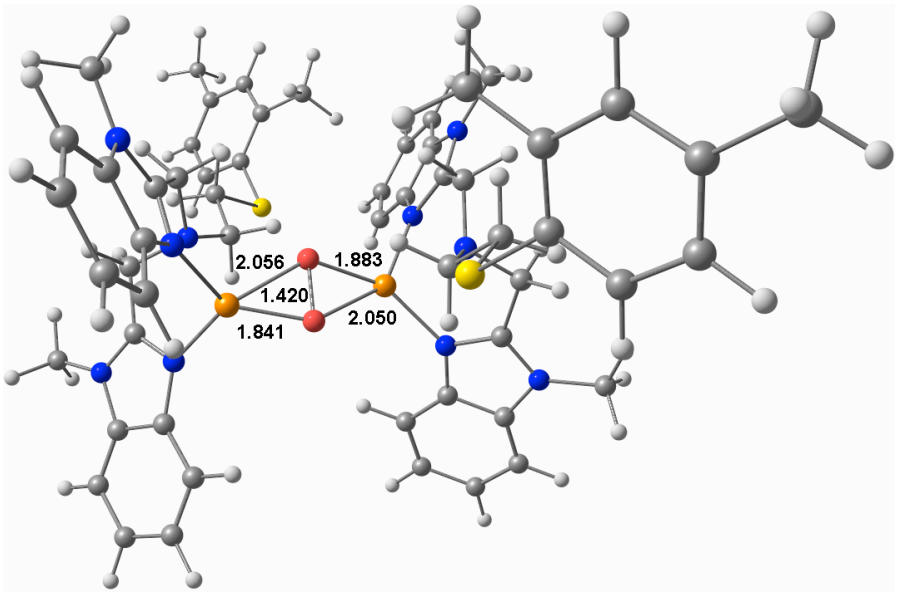

Figure S17. Optimised structure of singlet $[(\mathbf{L^1}Cu)_2\text{-}\mu\text{-}\eta^2\text{:}\eta^2\text{-}O_2]^{2+}$ (side-on peroxo, uncoordinated arylthioether) with interatomic distances.

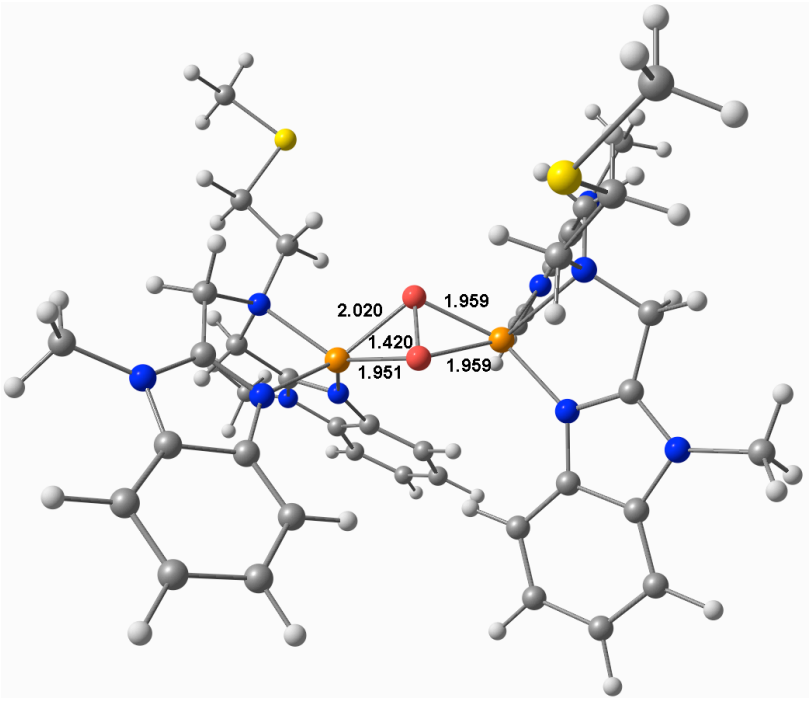

Figure S18. Optimised structure of singlet $[(\mathbf{L^2}Cu)_2\text{-}\mu\text{-}\eta^2\text{:}\eta^2\text{-}O_2]^{2+}$ (side-on peroxo, uncoordinated methylthioether) with interatomic distances.

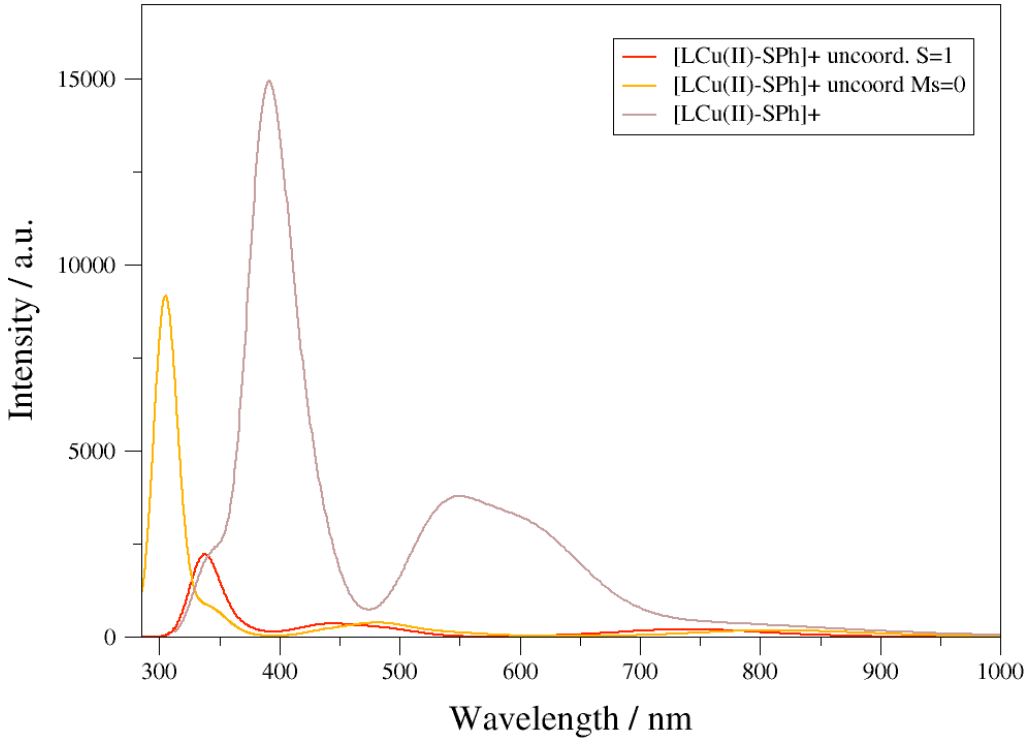

Figure S19. Theoretical fit by TD-DFT of electronic spectra of arylthioether-uncoordinated singlet $[(\mathbf{L^1}Cu)_2\text{-}\mu\text{-}\eta^2\text{:}\eta^2\text{-}O_2]^{2+}$ (tan), singlet side-on $[\mathbf{L^1}CuO_2]^{+}$ (yellow), and triplet side-on $[\mathbf{L^1}CuO_2]^{+}$ (red trace).

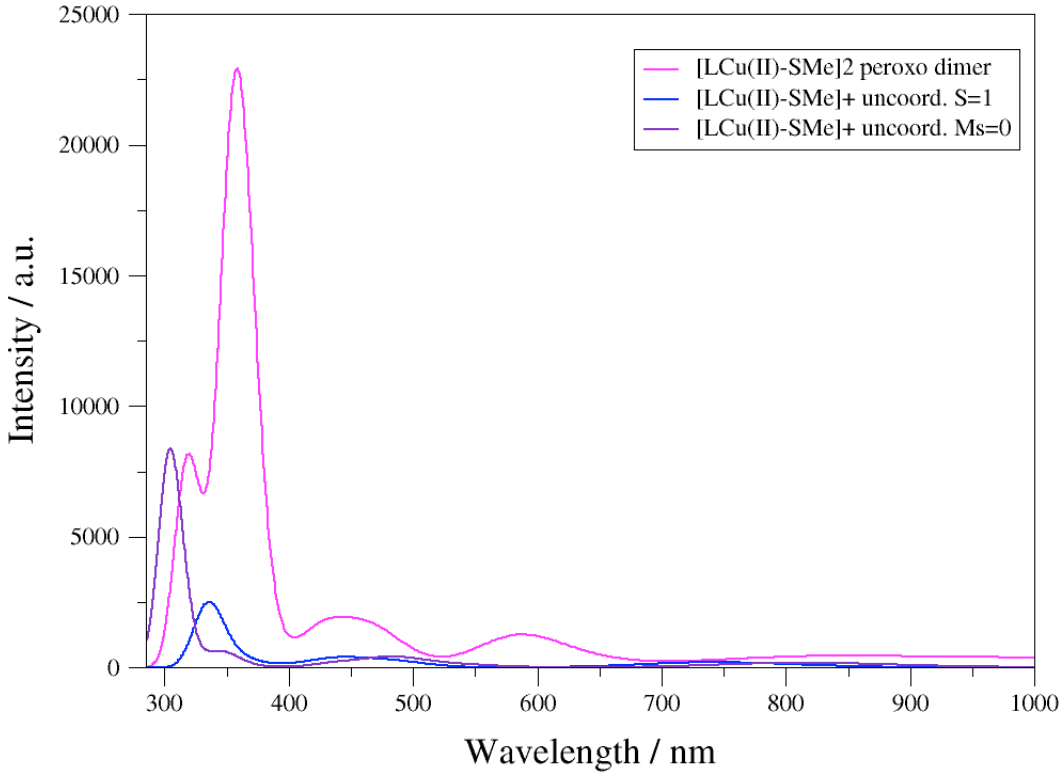

Figure S20. Theoretical fit by TD-DFT of electronic spectra of methylthioether-uncoordinated singlet $[(\mathbf{L^2}Cu)_2\text{-}\mu\text{-}\eta^2\text{:}\eta^2\text{-}O_2]^{2+}$ (pink), singlet side-on $[\mathbf{L^2}CuO_2]^+$ (purple), and triplet side-on $[\mathbf{L^2}CuO_2]^+$ (blue trace).

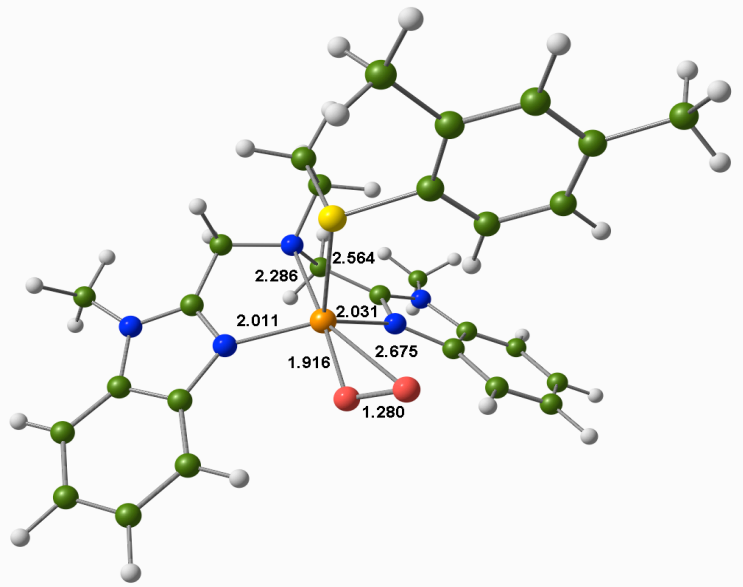

Figure S21. Optimised structure of triplet $[\mathbf{L^1}CuO_2]^+$ (end-on superoxo, coordinated arylthioether) with interatomic distances.

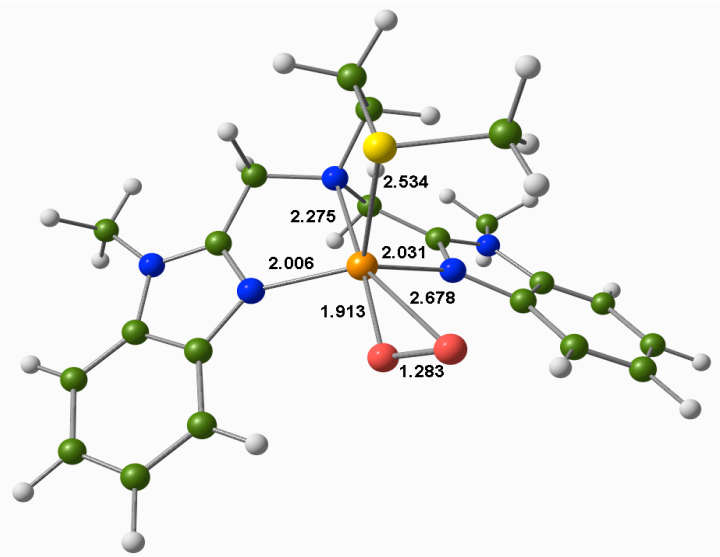

Figure S22. Optimised structure of triplet $[\mathbf{L}^{2}CuO_2]^+$ (end-on superoxo, coordinated methylthioether) with interatomic distances.

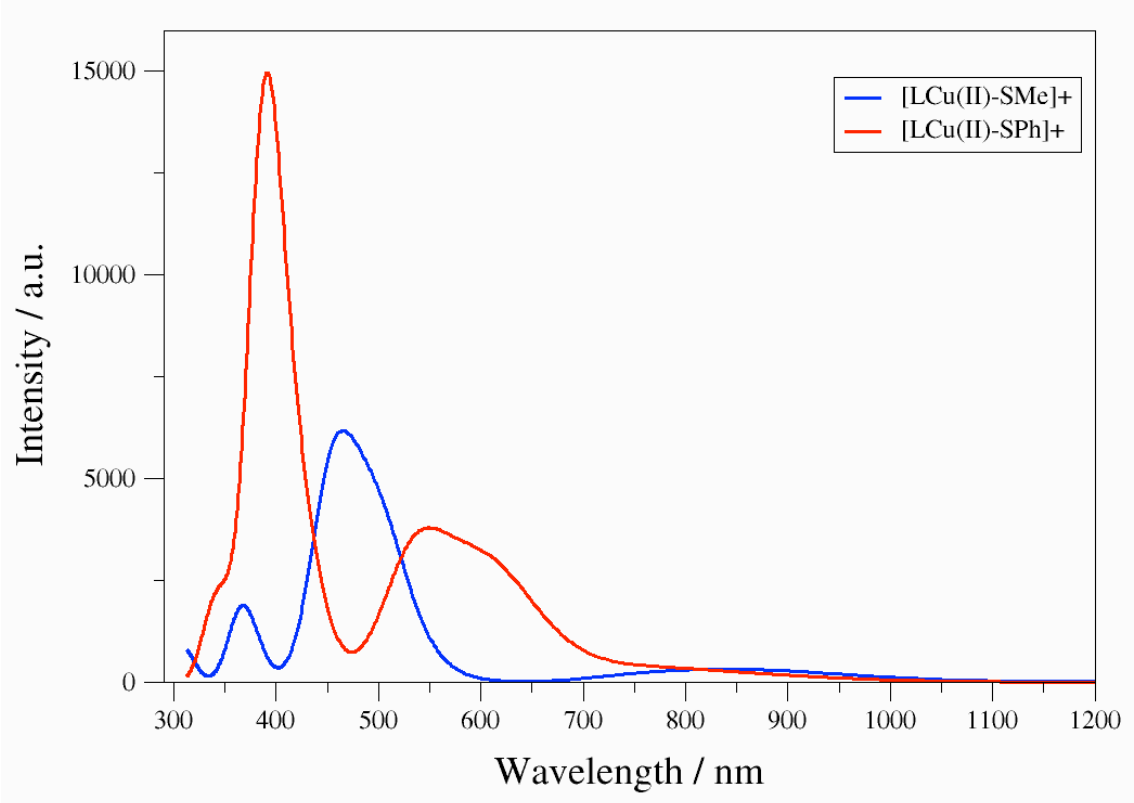

Figure S23. Theoretical fit by TD-DFT of electronic spectra of thioether-coordinated triplet $[\mathbf{L}^{1}CuO_2]^+$ (red trace, LCu^{II}-SAr), and triplet $[\mathbf{L}^{2}CuO_2]^+$ (blue trace, LCu^{II}-SMe).

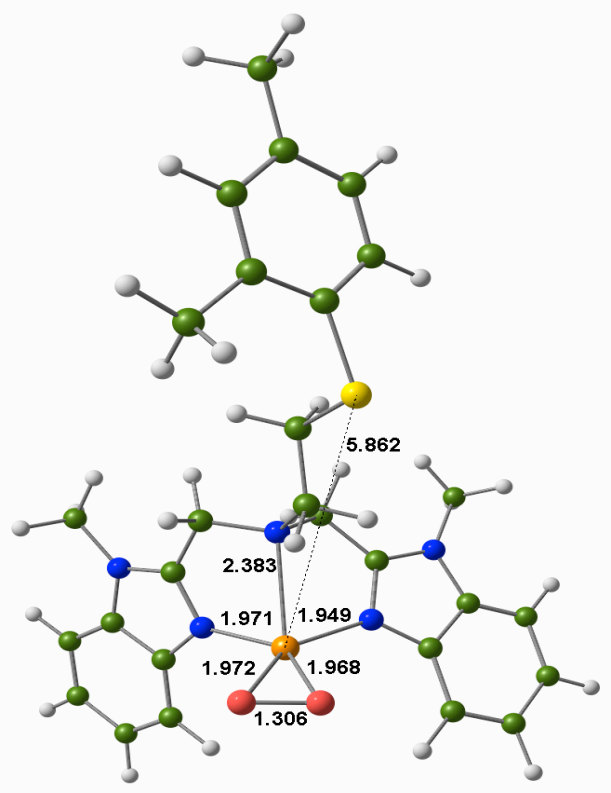

Figure S24. Optimised structure of triplet $[\mathbf{L}^{1}CuO_2]^+$ (side-on superoxo, uncoordinated arylthioether) with interatomic distances.

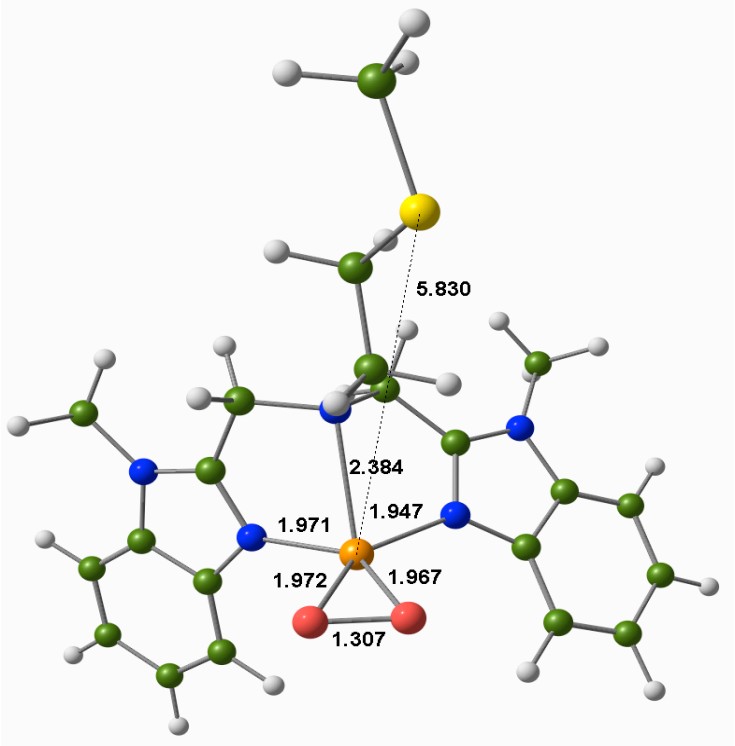

Figure S25. Optimised structure of triplet $[\mathbf{L}^{2}CuO_2]^+$ (side-on superoxo, uncoordinated methylthioether) with interatomic distances.

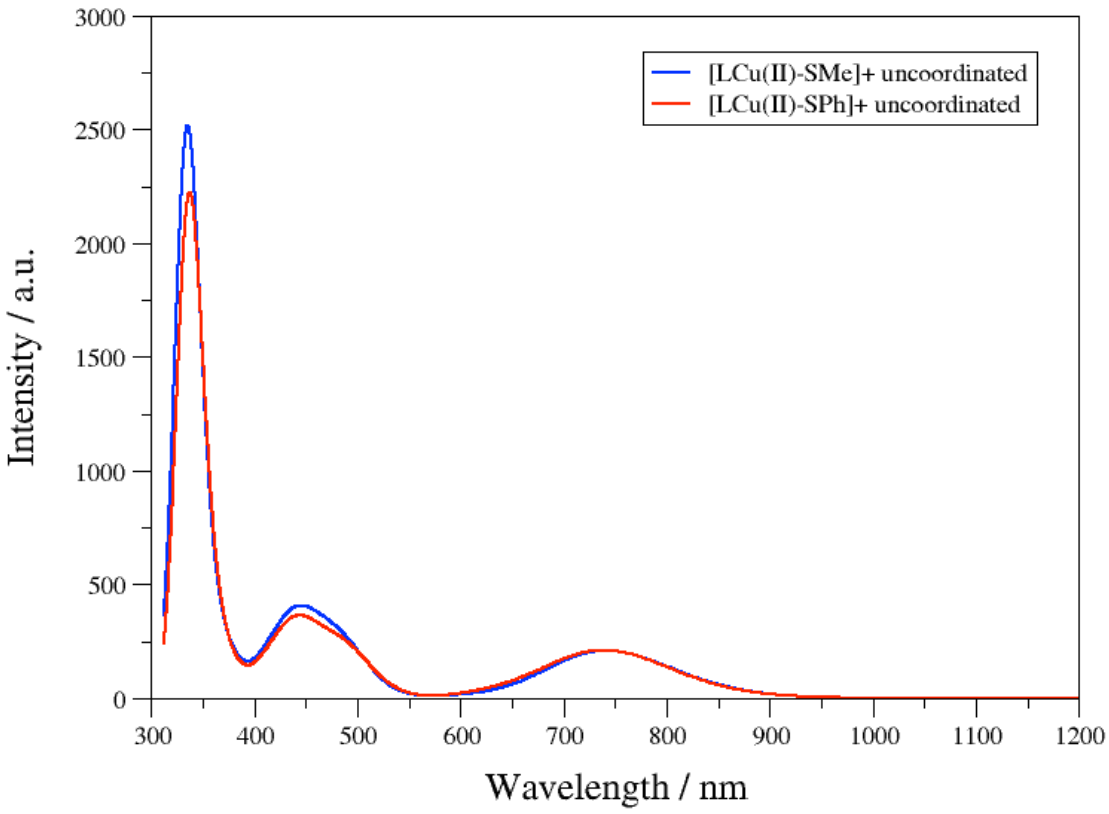

Figure S26. Theoretical fit by TD-DFT of electronic spectra of thioether-uncoordinated triplet $[\mathbf{L}^{1}CuO_2]^+$ (red trace, LCu^{II}-SAr), and triplet $[\mathbf{L}^{2}CuO_2]^+$ (blue trace, LCu^{II}-SMe).

Table S2. Selected parameters from the calculated UV-vis spectra of triplet $[\mathbf{L}^{1}CuO_2]^+$

State	Transition (MO number)	λ^{calc} (nm)	f^{calc}	Assignment
1	βHOMO-1 → βLUMO 144β → 146β	745	0.0022	ligand→ superoxo
2	βHOMO-2 → βLUMO+1 143β → 147β	488	0.0023	ligand→ metal/superoxo
3	βHOMO-4 → βLUMO+1 141β → 147β	444	0.0030	ligand → metal/superoxo
4	βHOMO-9 → βLUMO 136β → 146β	357	0.0035	metal → superoxo
5	βHOMO-10 → βLUMO 135β → 146β	338	0.0209	ligand → superoxo
6	βHOMO-11 → βLUMO 134β → 146β	330	0.0032	metal → superoxo

Figure S27. Difference electron density sketches of transitions 1-6 for triplet (S-uncoordinated) $[\mathbf{L^1}CuO_2]^+$ (yellow = negative, red = positive).

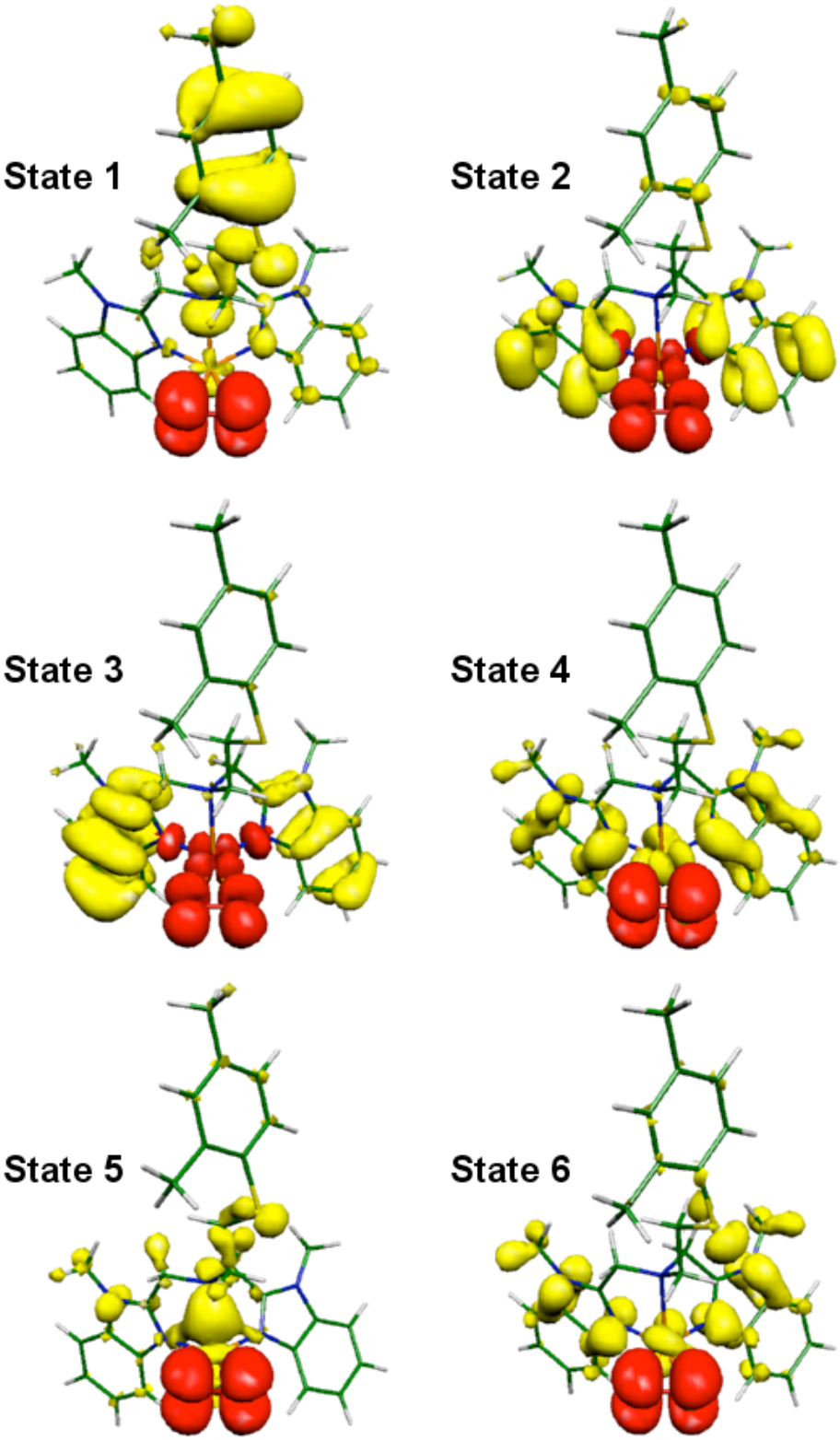

Table S3. Selected parameters from the calculated UV-vis spectra of triplet $[\mathbf{L}^{\mathbf{2}}CuO_2]^+$

State	Transition (MO number)	λ^{calc} (nm)	f^{calc}	Assignment
1	βHOMO-1 → βLUMO 120β → 123β	747	0.0022	ligand→ superoxo
2	βHOMO-2 → βLUMO+1 119β → 123β	489	0.0026	ligand→ metal/superoxo
3	βHOMO-4 → βLUMO+1 117β → 123β	444	0.0032	ligand → metal/superoxo
4	βHOMO-9 → βLUMO 112β → 122β	358	0.0030	metal→ superoxo
5	βHOMO-10 → βLUMO 111β → 122β	337	0.0220	metal → superoxo
6	βHOMO-11 → βLUMO 110β → 122β	329	0.0024	metal → superoxo

Figure S28. Difference electron density sketches of transitions 1-6 for triplet (S-uncoordinated) $[\mathbf{L}^{2}CuO_2]^{+}$ (yellow = negative, red = positive).

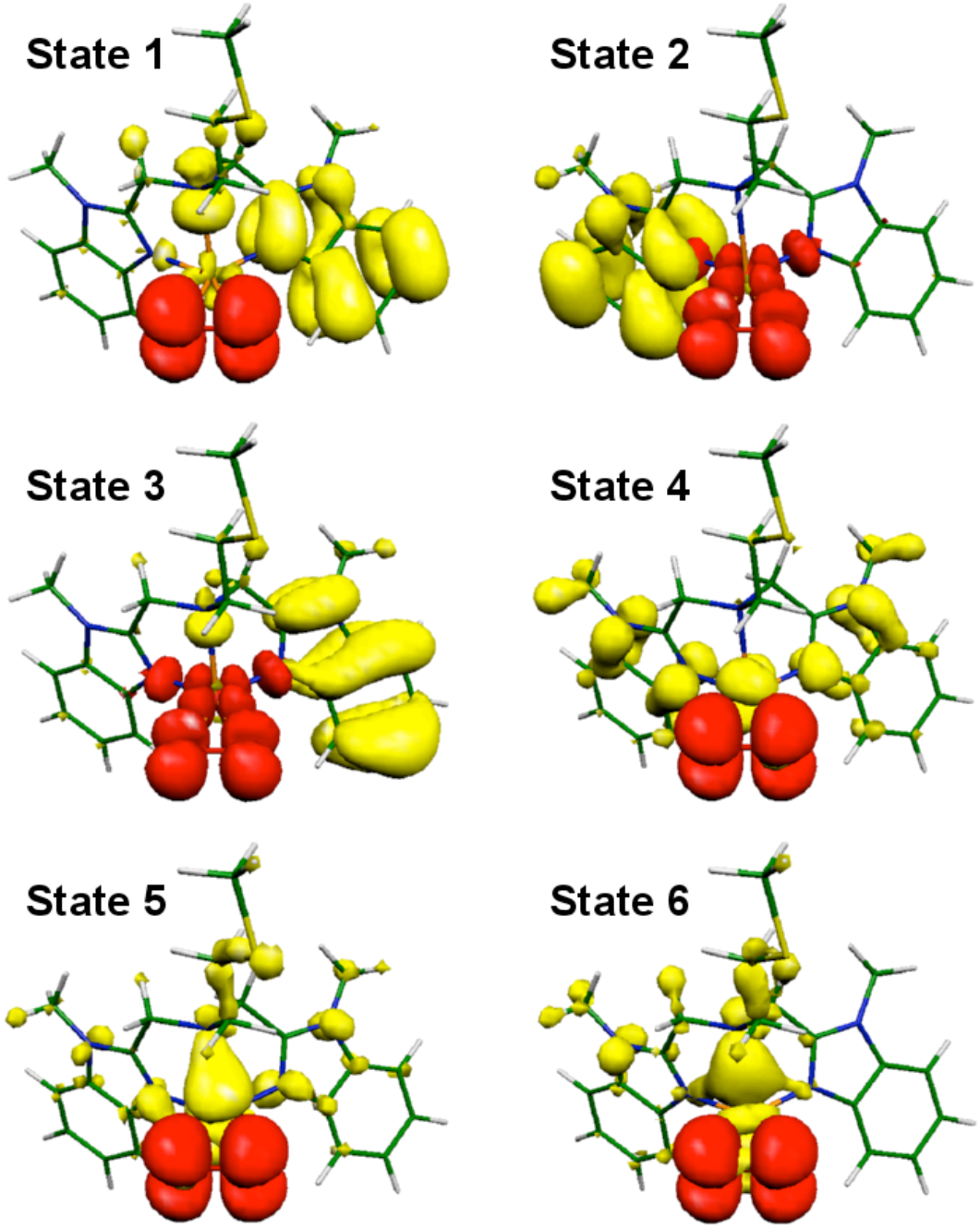

Table S4. Calculated exchange coupling constants (*J*) and spatial overlaps (*S*) for side-on superoxo $[\mathbf{L^1}CuO_2]^+$ and $[\mathbf{L^2}CuO_2]^+$ complexes with uncoordinated thioethers.

Species	$[\mathbf{L^1}CuO_2]^+$		$[\mathbf{L^2}CuO_2]^+$	
Spin state	S = 1	Ms = 0	S = 1	Ms = 0
Energy (Eh)	-3549.237226	-3549.235715	-3278.787038	-3278.785605
DE (kJ/mol)	0	+4.0	0	+3.8
J (cm^{-1})	249.9		236.8	
Spatial overlap *S*	0.56804		0.56993	
Magnetic coupling	ferromagnetic		ferromagnetic	
Ground spin state	Triplet		triplet	

Figure S29. Calculated spin ladder of side-on superoxo $[\mathbf{L^1}CuO_2]^+$ complex with uncoordinated arylthioether.

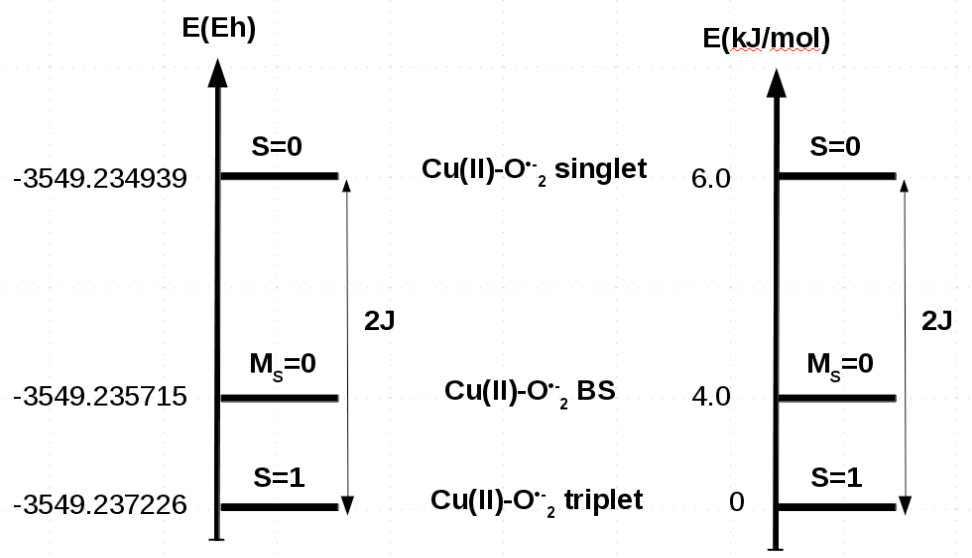

Figure S30. Calculated spin ladder of side-on superoxo $[\mathbf{L}^2CuO_2]^+$ complex with uncoordinated methylthioether.

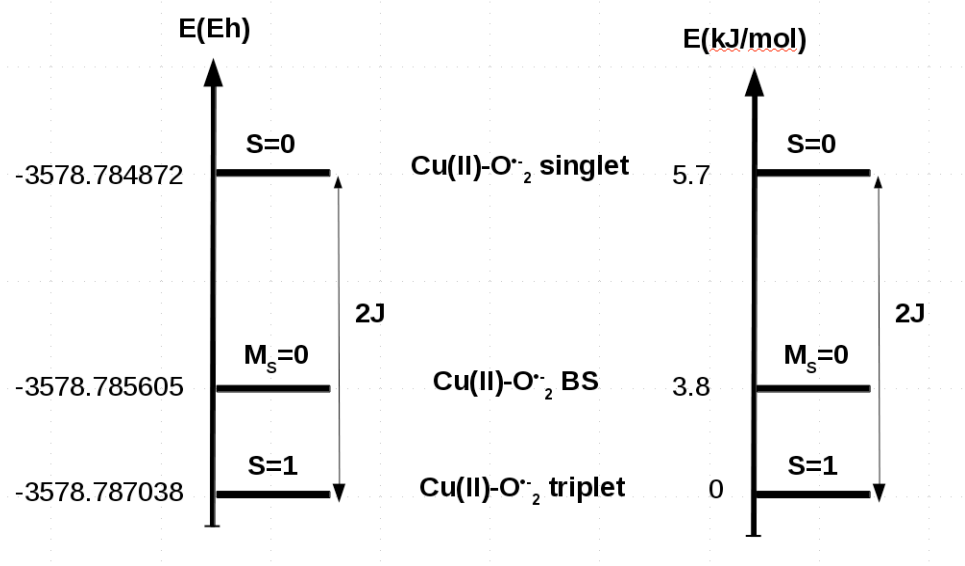

Figure S31. Spin population distribution and and magnetic orbitals of triplet (S-uncoordinated) $[\mathbf{L}^1CuO_2]^+$.

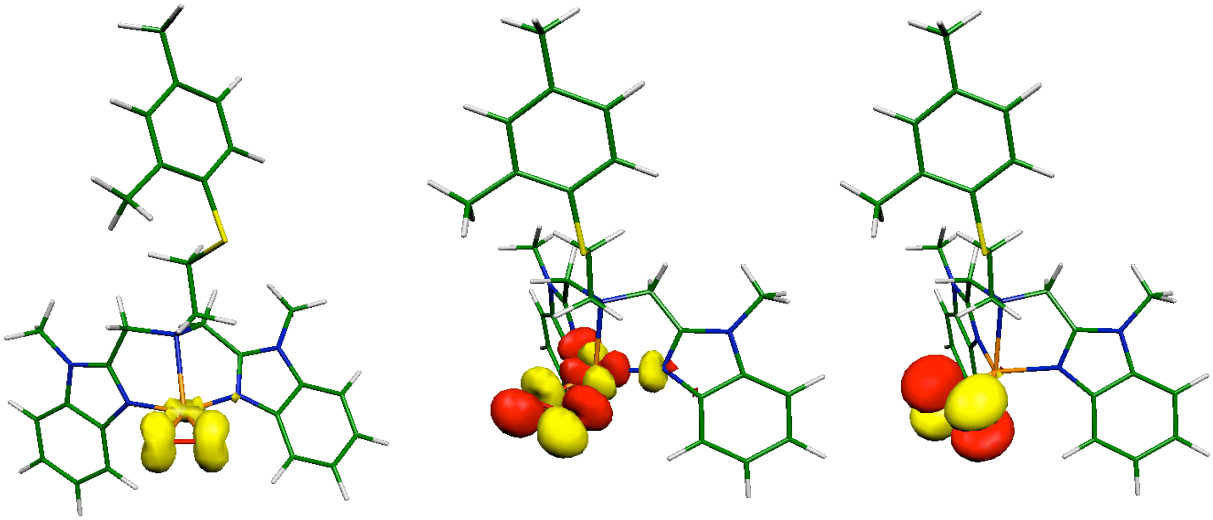

Composition of the SOMOs: 45% Cu, 46% O, 9% remaining & 1% Cu, 98% O, 1% remaining.

Figure S32. Spin population distribution and magnetic orbitals of triplet (S-uncoordinated) $[\mathbf{L}^{\mathbf{2}}CuO_2]^+$.

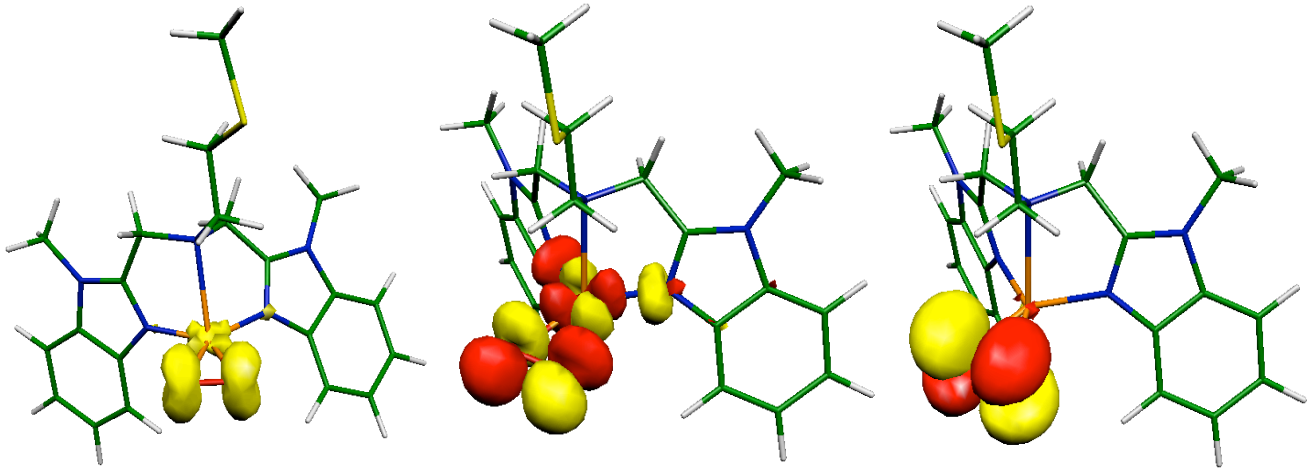

Composition of the SOMOs: 45% Cu, 46% O, 9% remaining & 1% Cu, 98% O, 1% remaining.

Figure S33. Molecular orbital diagram of triplet side-on superoxo $[\mathbf{L^1}CuO_2]^+$ with uncoordinated arylthioether. Color code: Cu, dark yellow; O, red; N, dark blue; C, green; H, white.

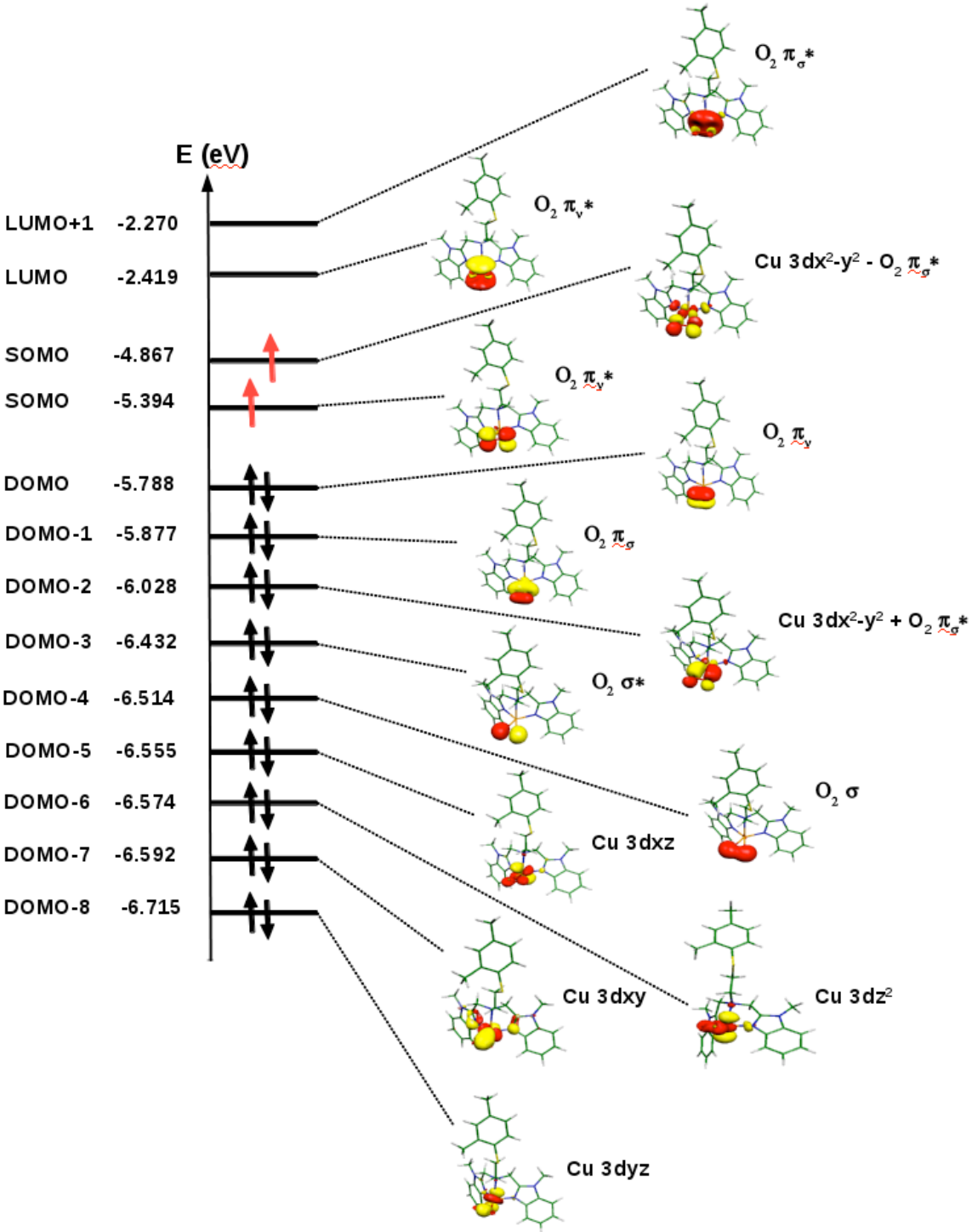

Figure S34. Molecular orbital diagram of triplet side-on superoxo $[\mathbf{L}^{2}CuO_2]^{+}$ with uncoordinated arylthioether. Color code: Cu, dark yellow; O, red; N, dark blue; C, green; H, white.

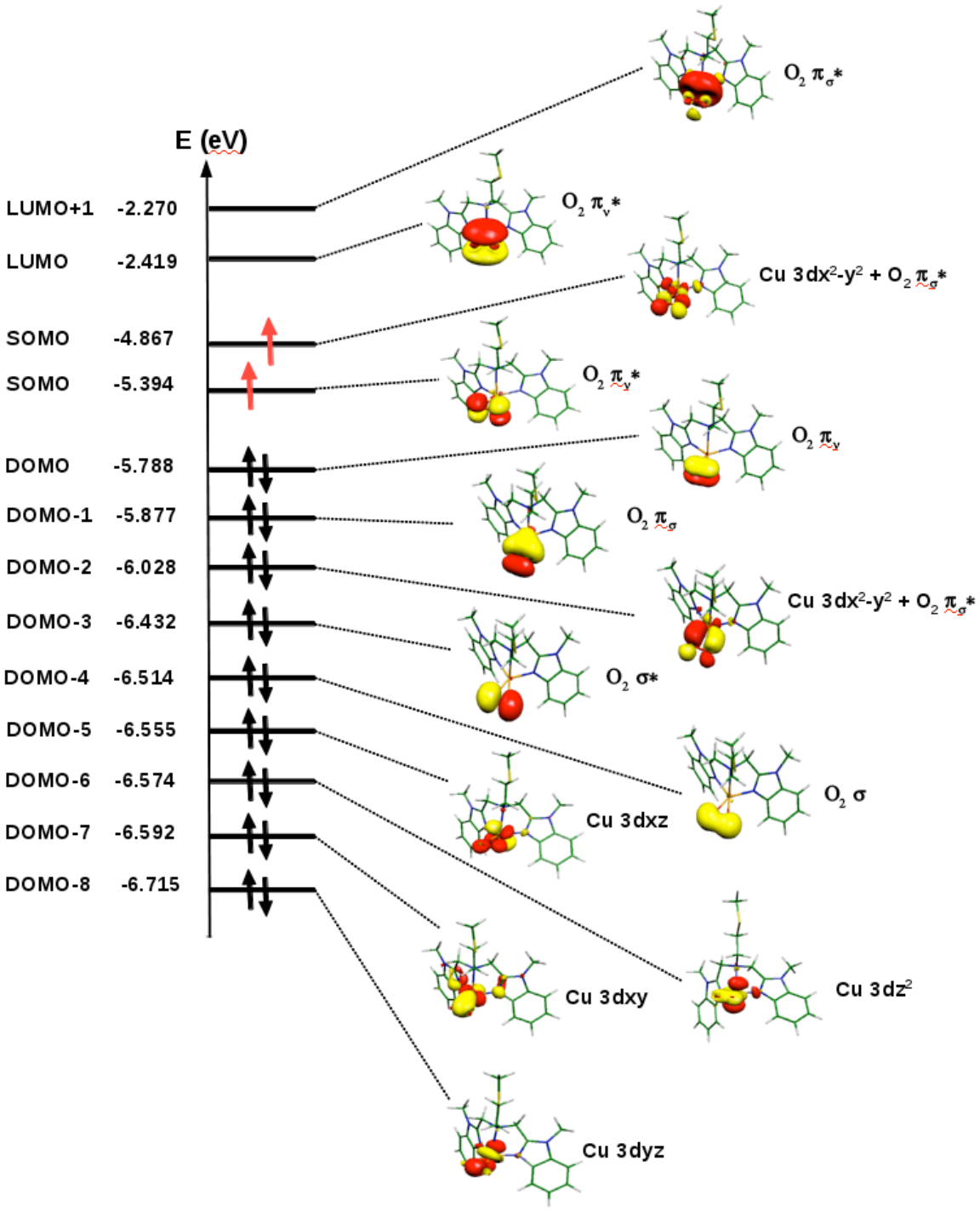

7. Characterisation of hydroperoxo complexes

The UV-vis spectra of hydroperoxo complexes were recorded at room temperature in THF, and analysed by ESR at liquid nitrogen temperature in anhydrous acetone. $\mathbf{L^1}Cu^{II}(CF_3SO_3)_2$ and $[\mathbf{L^2}Cu^{II}Cl]ClO_4$ were dissolved in acetone and cooled to -80°C in a Dewar, and 5 equiv of a 1:1 H_2O_2/Et_3N acetone solution was added prior to the ESR measurements.

$[\mathbf{L^1}Cu^{II}–OOH]^+$. UV-vis (25°C, THF): λ = 309 nm, ε = 1279 M^{-1} cm^{-1}; λ = 339 nm, ε = 1146 M^{-1} cm^{-1}. λ = 324 nm, ε = 1099 M^{-1} cm^{-1}; *d-d* = 712 nm, ε = 145 M^{-1} cm^{-1}. ESR (77 K, CH_3COCH_3): $g_{\parallel}$ = 2.273; $g_{\perp}$ = 2.053; $A_{\parallel}$ = 157 G.

$[\mathbf{L^2}Cu^{II}–OOH]^+$. UV-vis (25°C, THF): λ = 305 nm, ε = 1780 M^{-1} cm^{-1}; *d-d* λ = 737 nm, ε = 115 M^{-1} cm^{-1}. ESR (77K, CH_3COCH_3): $g_{\parallel}$ = 2.256; $g_{\perp}$ = 2.056; $A_{\parallel}$ = 169 G.

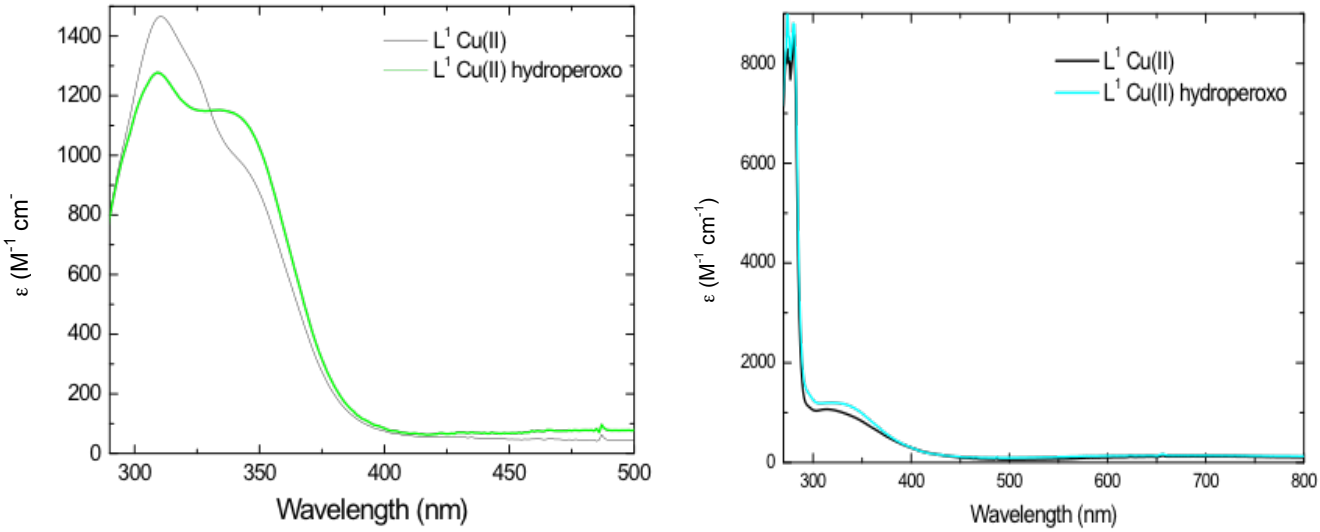

Figure S35. UV-vis spectra of hydroperoxo complex $[\mathbf{L^1}Cu^{II}–OOH]^+$ (THF, RT).

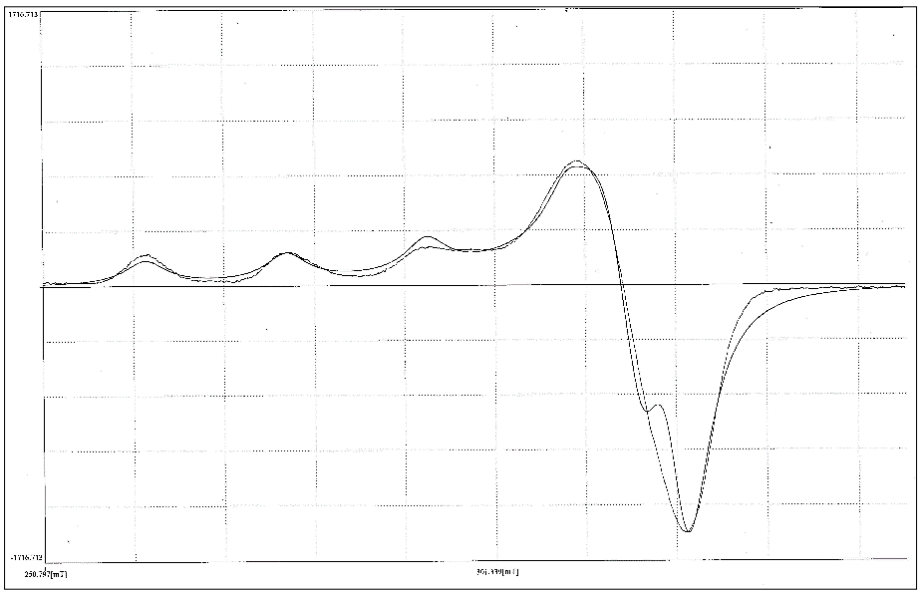

Figure S36. Experimental and simulated ESR spectra of $[\mathbf{L^1}Cu^{II}–OOH]^+$ (Acetone, 77 K).

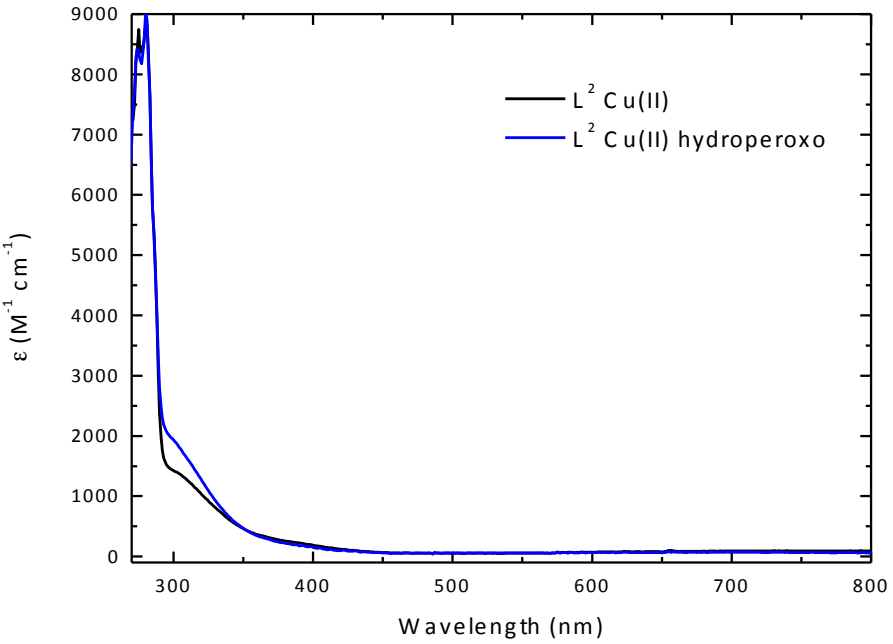

Figure S37. UV-vis spectra of hydroperoxo complex of $[\mathbf{L^2}Cu^{II}–OOH]^+$ (THF, RT).

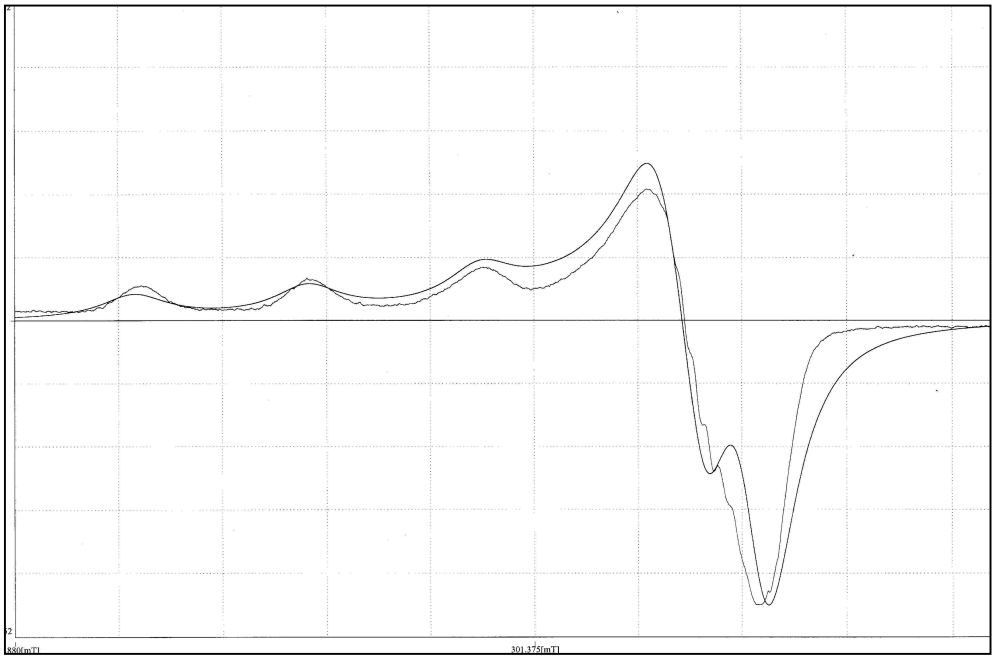

Figure S38. Experimental and simulated ESR spectra of $[\mathbf{L^2}Cu^{II}–OOH]^+$ (Acetone, 77 K).

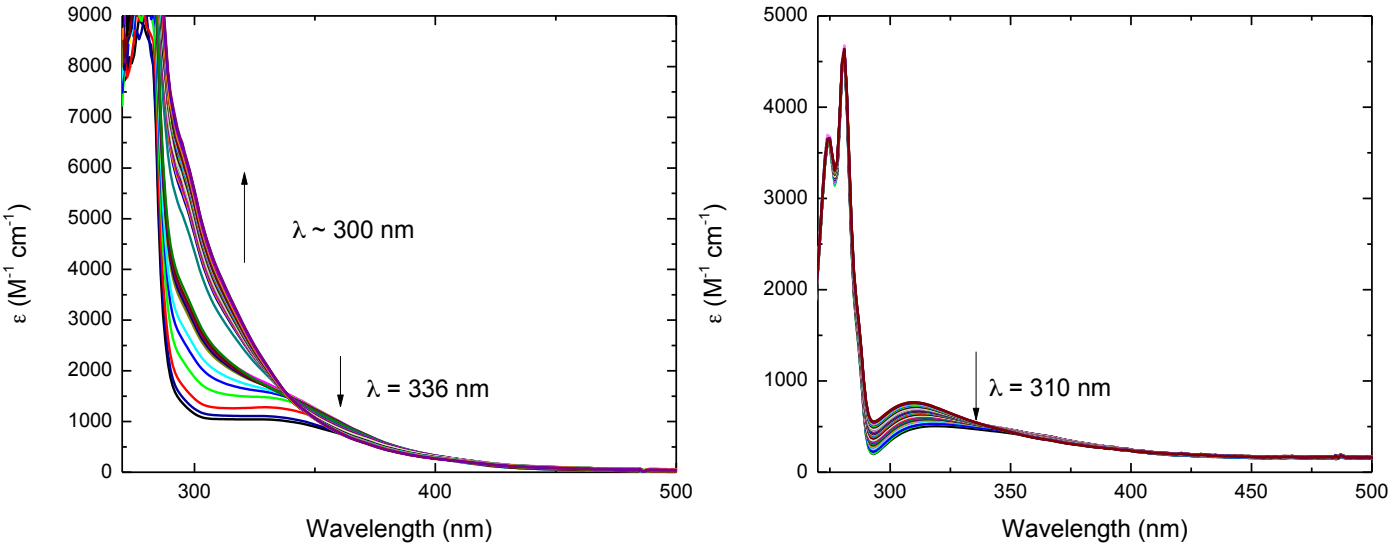

Figure S39. UV-vis spectra of thermal decomposition of [(**L**^{1} (left)/**L**^{2} (right))Cu^{II}–OOH]$^{+}$ in THF at 40°C.

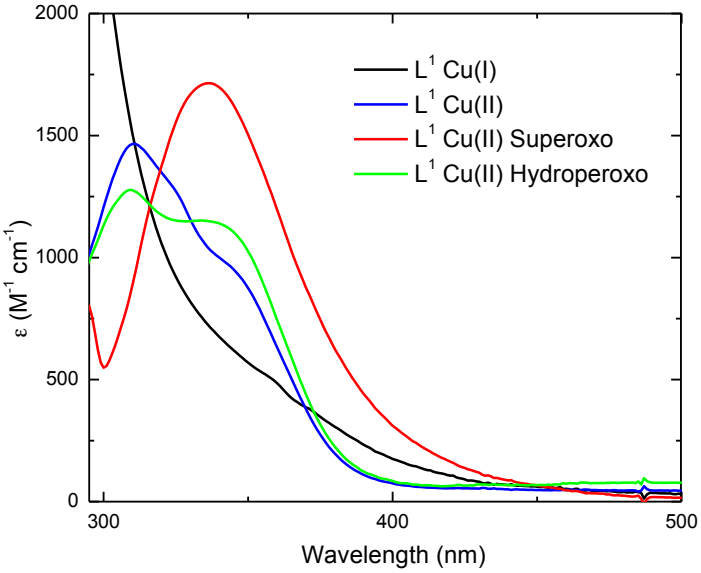

Figure S40. Comparison of electronic spectra of **L**^{1} complexes (THF, RT except for the superoxo complex acquired at -80°C).

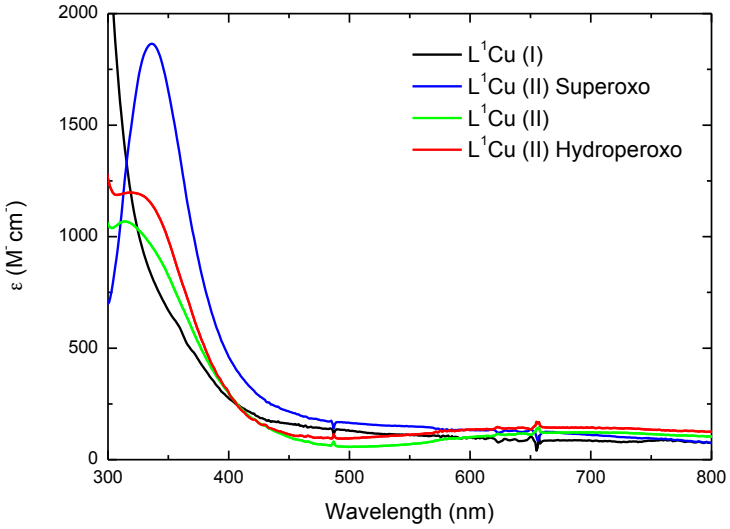

Figure S41. Comparison of full electronic spectra of **L**[1] complexes (THF, RT except for the superoxo complex acquired at -80°C).

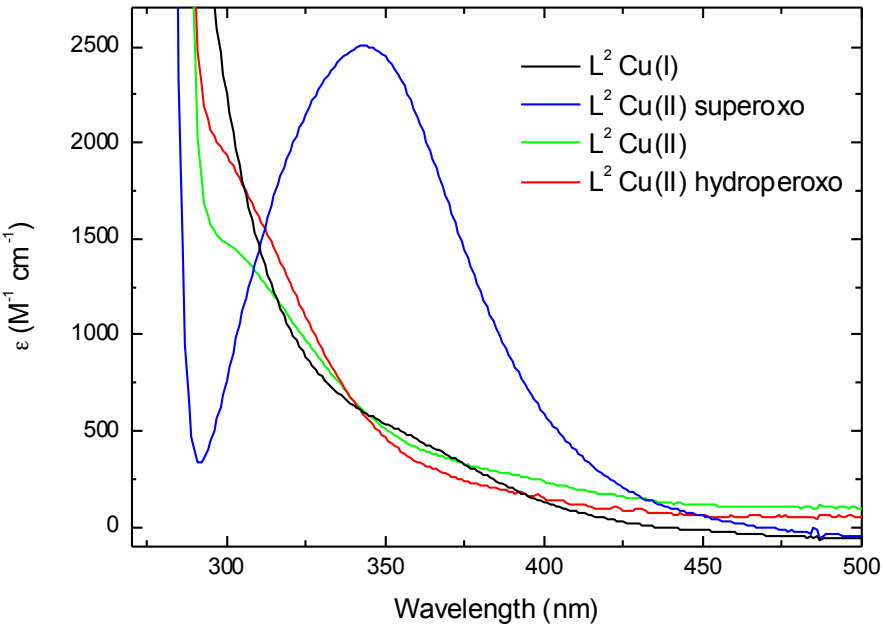

Figure S42. Comparison of electronic spectra of **L**[2] complexes (THF, RT except for the superoxo).

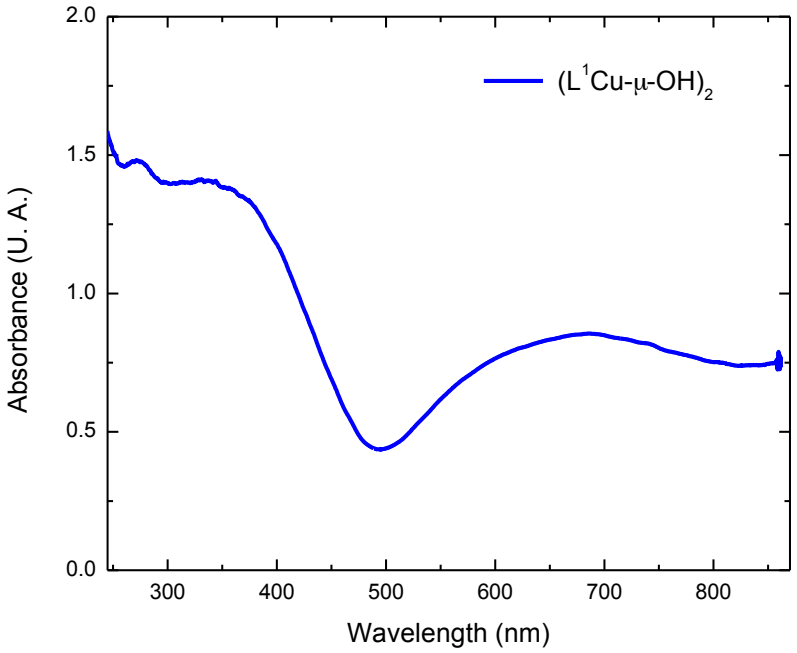

Figure S43. Diffuse reflectance UV-vis spectra of $[\mathbf{L^1}Cu(\mu–OH)]_2OTf_2$.

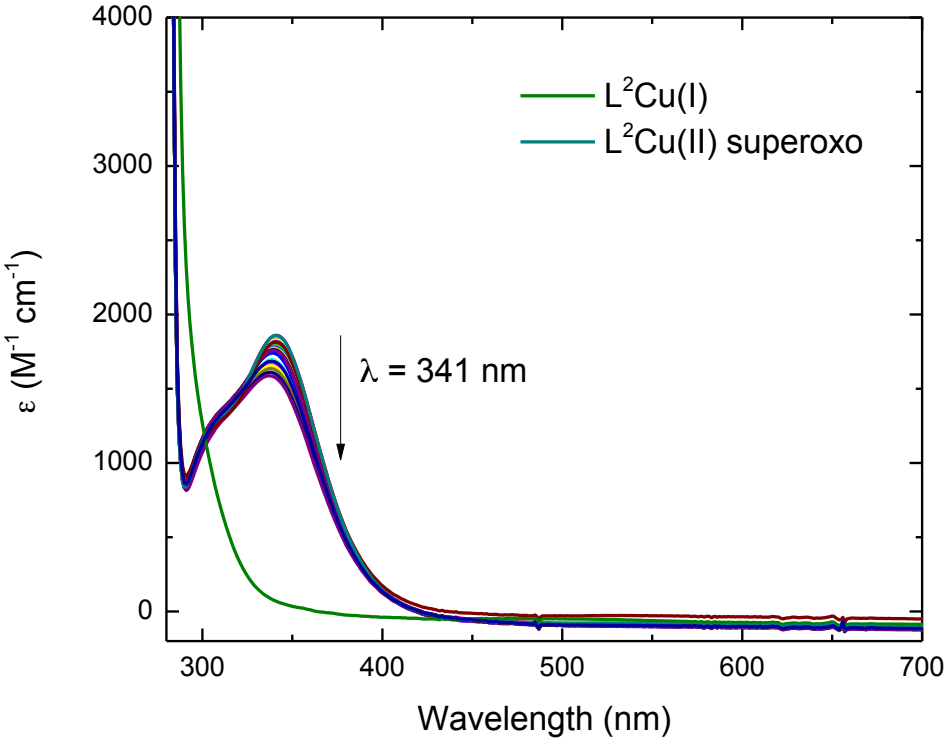

Figure S44. UV-vis spectra of the disappearance of the band of $[\mathbf{L^2}Cu^{II}O_2^{\cdot-}]^+$ at 341 nm (THF, -40°C).

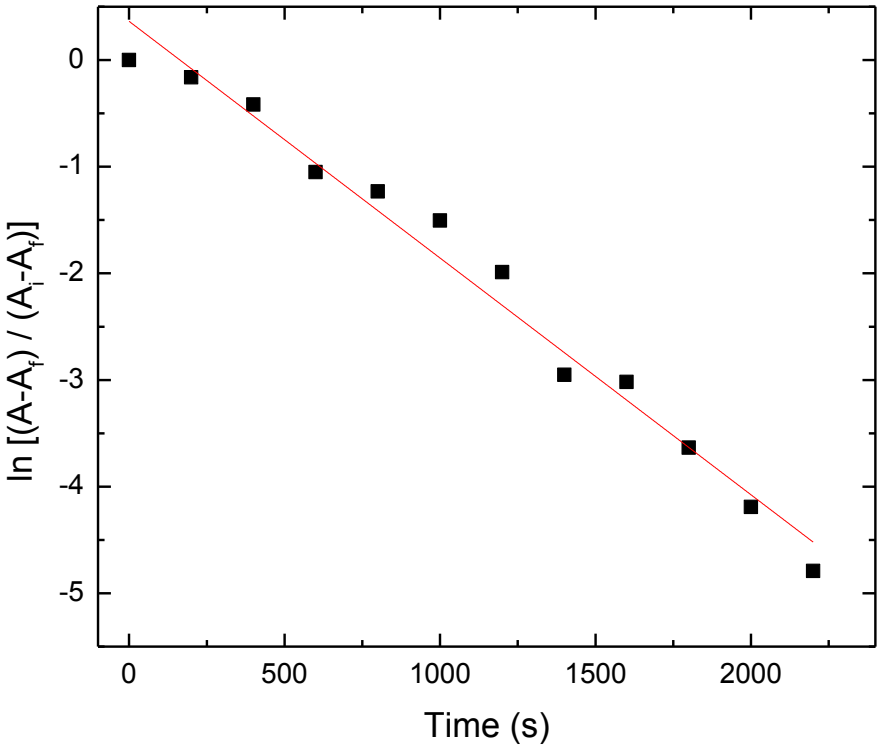

Figure S45. Pseudo first-order rate plot of the disappearance of 341 nm band of complex $[\mathbf{L}^{2}Cu^{II}O_{2}^{\cdot -}]^{+}$ (THF at -40°C), R = 0.99

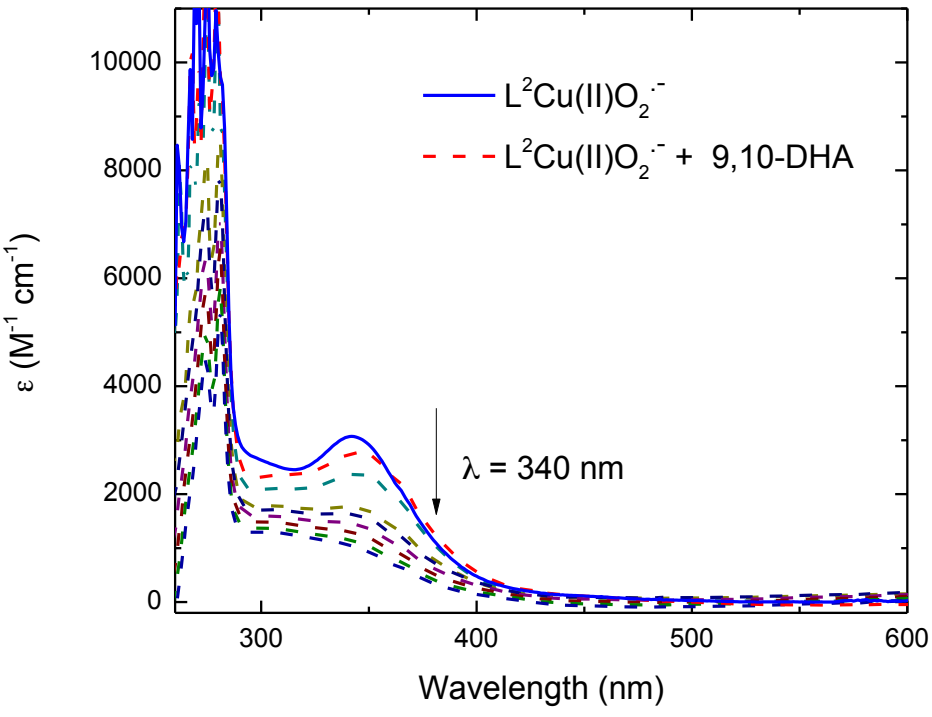

Figure S46. UV-vis spectra of $[\mathbf{L}^{2}Cu^{II}O_{2}^{\cdot -}]^{+}$ with 9,10-DHA (THF, -60°C).

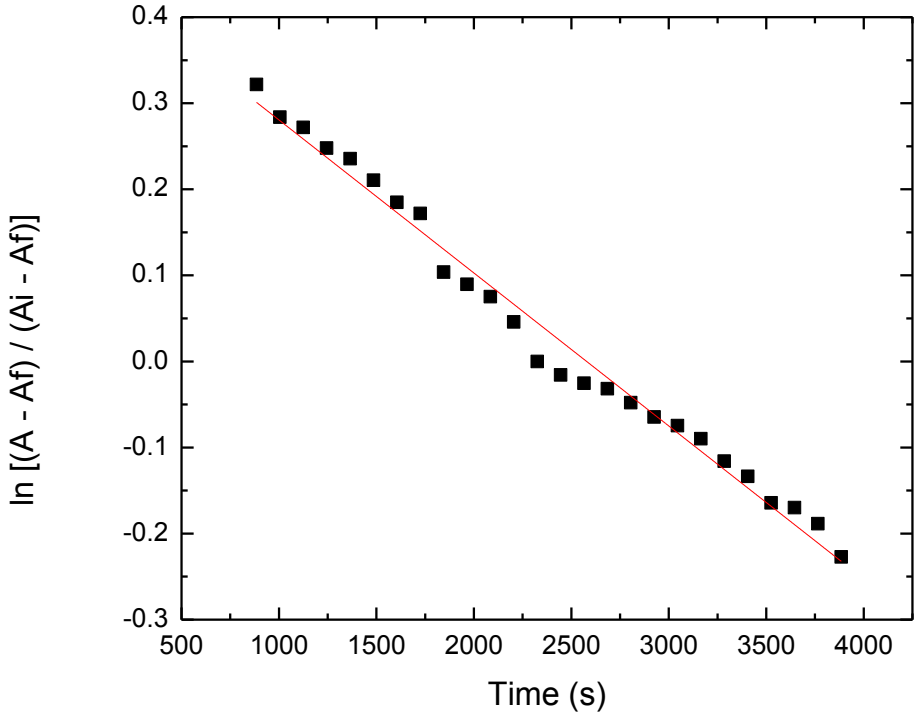

Figure S47. Pseudo first-order rate plot of the disappearance of 340 nm band of complex $[\mathbf{L^2}Cu^{II}O_2^{\cdot-}]^+$ with 9,10-DHA (THF, -60°C), R = 0.98

8. Characterisation of products from reactivity studies

Once the Cu/O_2 species were generated (superoxo and hydroperoxo), in the glovebox a 3 mM solution of 9,10-DHA was prepared in 10 mL of THF; 0.1 mL of this solution (1:10 copper/substrate ratio) was added to the solution containing the reactive copper-oxygen species. After 1 hour of reaction, a liquid-liquid extraction with 0.5 M EDTA solution and CH_2Cl_2 was done by triplicate. The organic extract was analyzed by GC-MS, the sample was dissolved in 1 mL CH_2Cl_2 and 1 µL was injected.

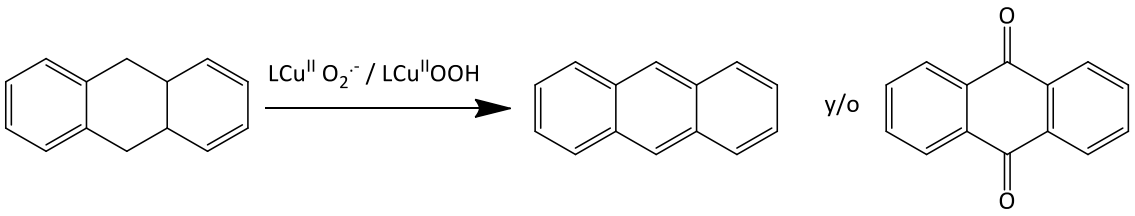

Scheme S1. Products from the reaction of $[\mathbf{L^1}\text{-}\mathbf{L^2}Cu^{II}\text{–}OO^{\bullet-}$ / $\mathbf{L^1}\text{-}\mathbf{L^2}Cu^{II}\text{–}OOH]^+$ with 9,10-DHA.

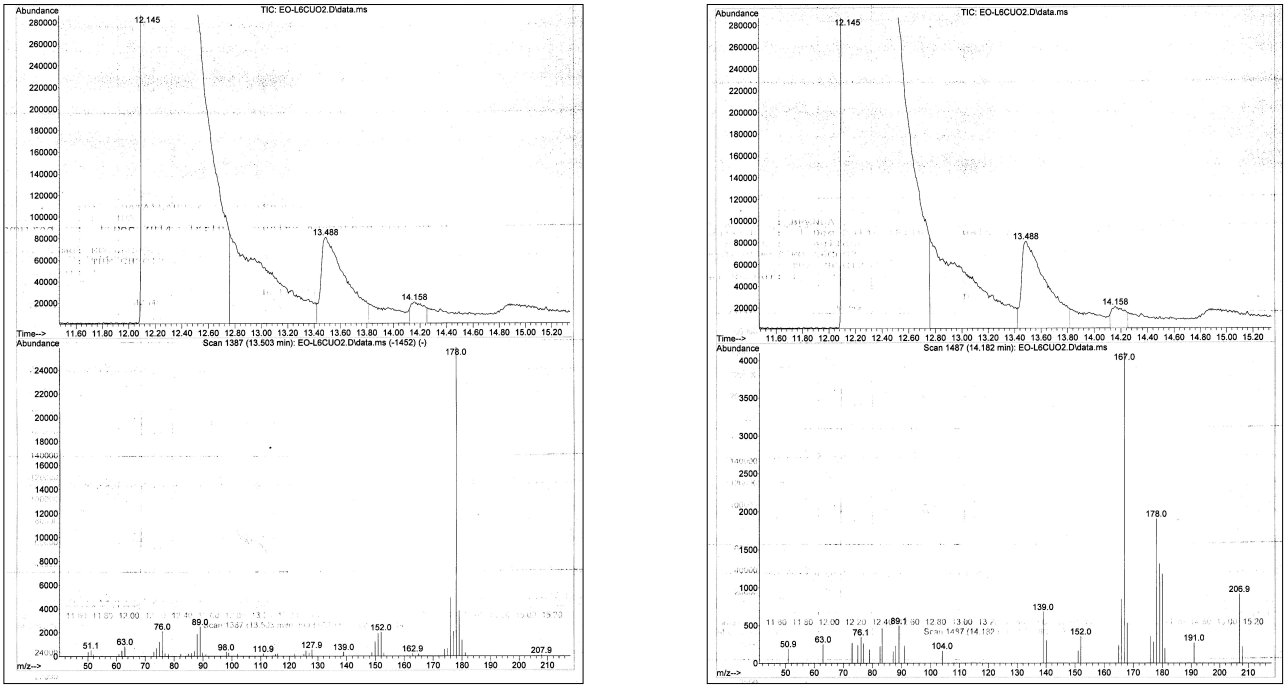

Figure S48. TIC/GC-MS of the product from the reaction of $\mathbf{L^1}Cu^{II}–OO^{\bullet-}$ with 9,10-DHA. All the spectra on the left correspond to the anthracene profile, and the ones on the right correspond to the anthraquinone profile.

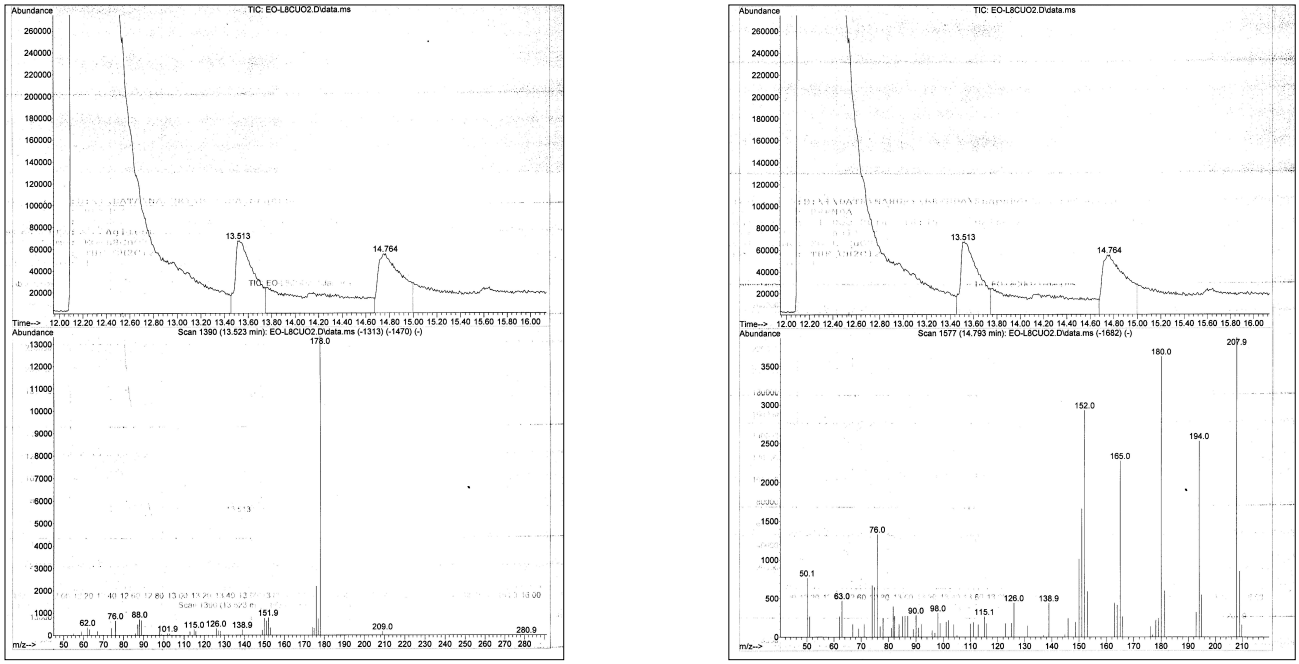

Figure S49. TIC/GC-MS of the product from the reaction of $\mathbf{L^2}Cu^{II}–OO^{\bullet-}$ with DHA.

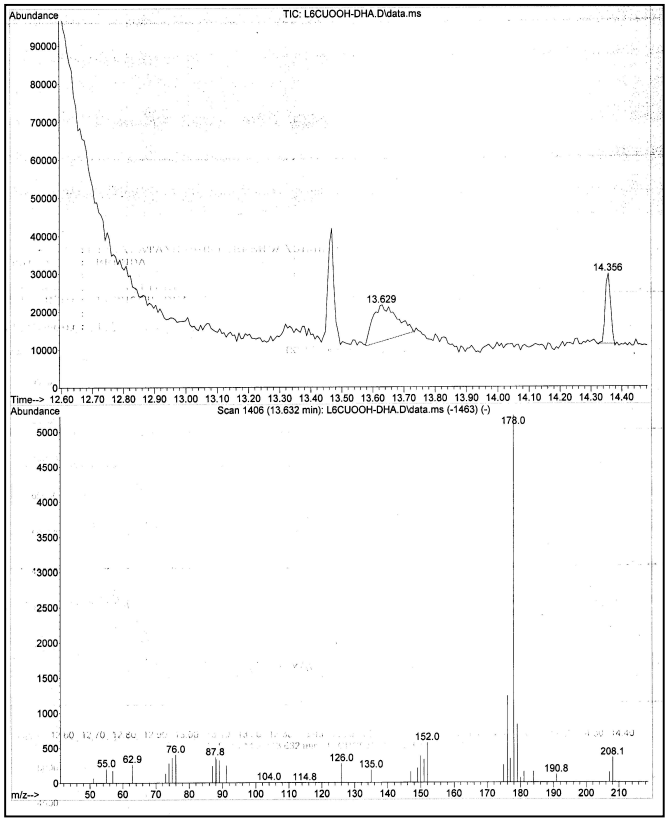

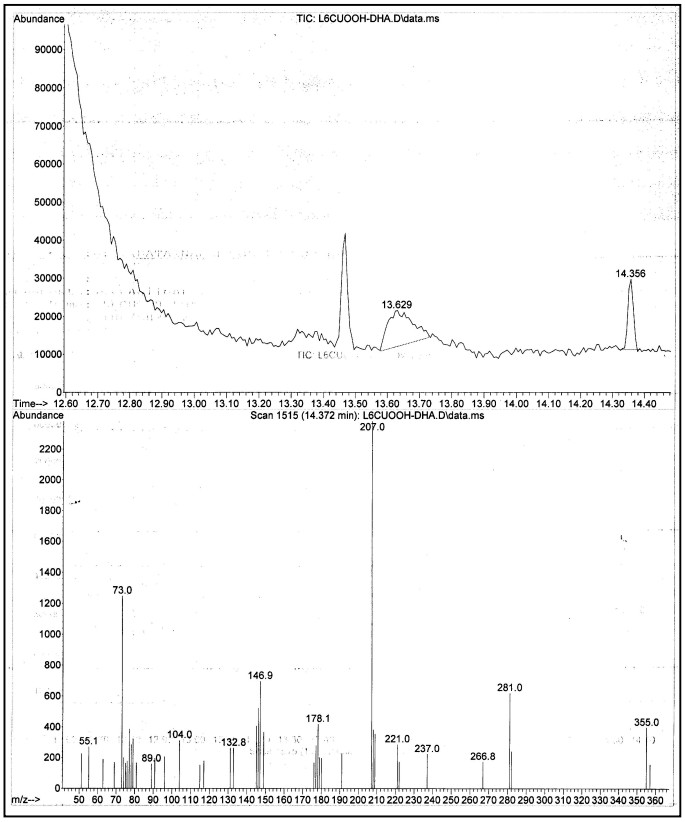

Figure S50. TIC/GC-MS of the product from the reaction of $\mathbf{L^1}Cu^{II}$–OOH with DHA.

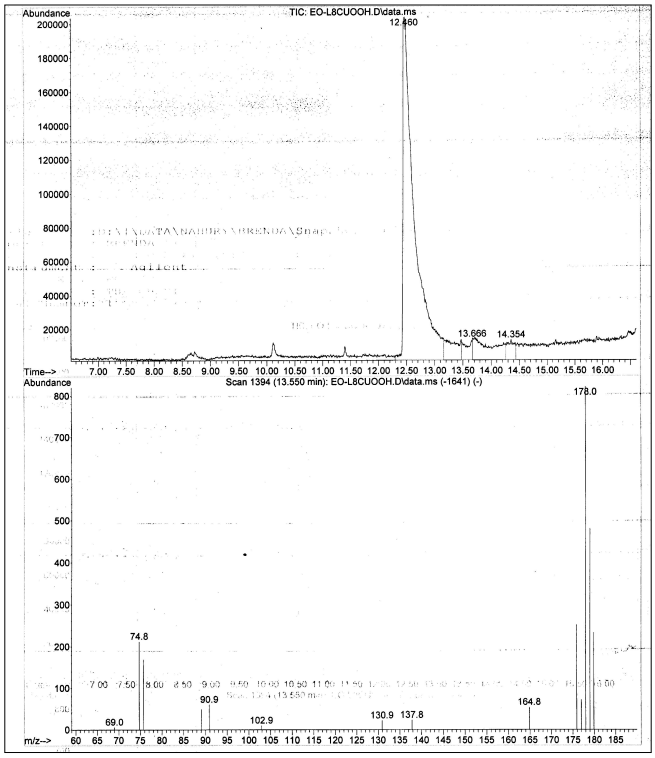

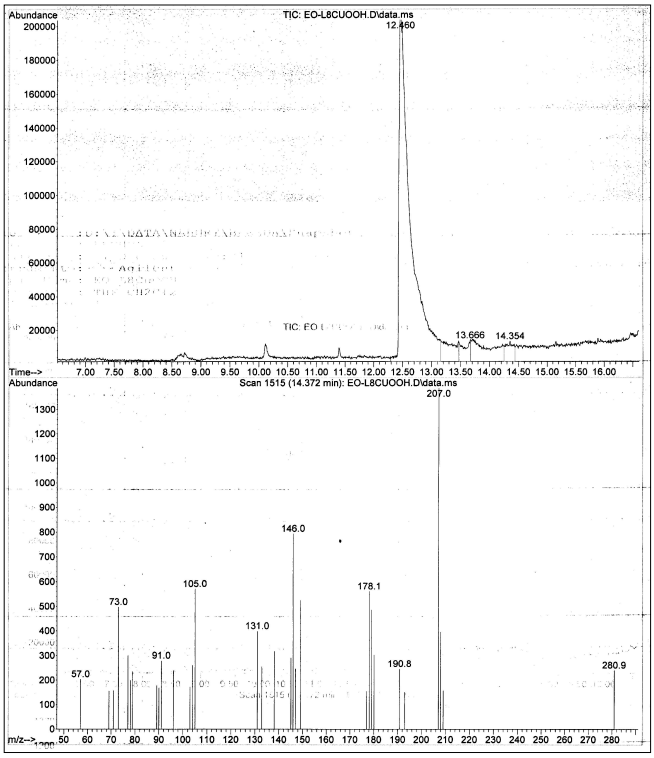

Figure S51. TIC/GC-MS of the product from the reaction of $\mathbf{L^2}Cu^{II}$–OOH with DHA.

9. References

(1) J. K. Irangu, R. B. Jordan, *Inorg. Chem*. 2003, **42**, 3934.

(2) (a) I. Castillo, V. M. Ugalde-Saldívar, L. A. Rodríguez Solano, B. N. Sánchez-Eguía, E. Zeglio, E. Nordlander, *Dalton Trans*. 2012, **41**, 9394; (b) I. Castillo, B. N. Sánchez-Eguía, V. M. Ugalde-Saldívar, P. R. Martínez-Alanís, M. Flores-Alamo, *Polyhedron*, 2015, **85**, 824.

(3) Bruker AXS, SAINT Software reference manual v. 6.23C, Madison, Wisconsin, USA, 2002.

(4) CRYSALIS CCD and CRYSALIS R, Oxford Diffraction, Abingdon, UK, 2009.

(5) G. M. Sheldrick, SHELXS-97, Crystal Structure Solution, University of Göttingen, Germany, 1990.

(6) G. M. Sheldrick, SHELXL-97, Crystal Structure Refinement, University of Göttingen, Germany, 1997.

(7) F. Neese, *Wiley Interdiscip. Rev. Comput. Mol. Sci.* 2012, **2**, 73.

(8) J. P. Perdew, *Phys. Rev. B* 1986, **33**, 8822.

(9) J. P. Perdew, *Phys. Rev. B* 1986, **34**, 7406.

(10) A. D. Becke, *Phys. Rev. A* 1988, **38**, 3098.

(11) A. Schäfer, C. Huber, R. Ahlrichs, *J. Chem. Phys*. 1994, **100**, 5829.

(12) F. Neese, *J. Comput. Chem.* 2003, **24**, 1740.

(13) F. Weigend, *PhysChemChemPhy*s 2006, **8**, 1057.

(14) A. Klamt, G. Schürmann, *J. Chem. Soc., Perkin Trans. 2* 1993, 799.

(15) A. D. Becke, *J. Chem. Phys.* 1993, **98**, 5648.

(16) C. T. Lee, W. T. Yang, R. G. Parr, *Phys. Rev. B* 1988, **37**, 785.

(17) M. E. Casida *in Recent Advances in Density Functional Methods,* D. P. Chong, Ed. World Scientific: Singapore, 1995.

(18) R. E. Stratmann, G. E. Scuseria, M. J. Frisch, *J. Chem. Phys.* 1998, **109**, 8218.

(19) R. Bauernschmitt, R. Ahlrichs, *Chem. Phys. Lett.* 1996, 454.

(20) S. Hirata, M. Head-Gordon, *Chem. Phys. Lett.* 1999, **314**, 291.

(21) S. Hirata, M. Head-Gordon, *Chem. Phys. Lett.* 1999, **302**, 375.

(22) F. Neese, *J. Chem. Phys*. 2001, **115**, 11080.

(23) Chemcraft http://chemcraftprog.com.

(24) L. Noodleman, *J. Chem. Phys.* **1981,** *74*, 5737.

(25) L. Noodleman, D. A. Case, *Adv. Inorg. Chem.* **1992,** *38*, 423.

(26) L. Noodleman, E. R. Davidson, *Chem. Phys.* **1986,** *109*, 131.

(27) T. Soda, Y. Kitagawa, T. Onishi, Y. Takano, Y. Shigeta, H. Nagao, Y. Yoshika, K. Yamaguchi, *Chem. Phys. Letters* **2000**, 223.

(28) K. Yamaguchi, Y. Takahara, T. Fueno, In *Applied Quantum Chemistry*, *V*, V. H. Smith, Ed., Reidel: Dordrecht, 1986.

(29) W. Heisenberg, *Z. Physik* **1926,** *38*, 411.

(30) W. Heisenberg, *Z. Physik* **1928,** *49*, 619.

(31) P. A. M. Dirac, *Proc. Roy. Soc.* **1929,** *A123*, 714.

(32) J. H. Van Vleck, *The Theory of Electronic and Magnetic Susceptibilies*. Oxford University: London 1932.